CUKUROVA UNIVERSITY
INSTITUTE OF NATURAL AND APPLIED SCIENCES

PhD THESIS

Teoman ÖZDAL

SPIN COATED CZTS SOLAR CELLS AND ANALYTICAL MODELLING

DEPARTMENT OF PHYSICS

ADANA-2020

ABSTRACT

PhD THESIS

SPIN COATED CZTS SOLAR CELLS AND ANALYTICAL MODELLING

Teoman ÖZDAL

CUKUROVA UNIVERSITY
INSTITUTE OF NATURAL AND APPLIED SCIENCES
DEPARTMENT OF PHYSICS

Supervisor : Prof. Dr. Hamide KAVAK
Year: 2020, Pages: 85
Jury : Prof. Dr. Hamide KAVAK
: Prof.Dr. Gülfeza KARDAŞ
: Assoc.Prof. Mustafa GÜNEŞ
: Asst.Prof.Dr. Şadi YILMAZ
: Asst.Prof.Dr. Mehmet Ali OLĞAR

Photoactive copper zinc tin sulfide (Cu_2ZnSnS_4, CZTS) semiconductors have been widely studied recently due to the advantages of low-cost, high absorption coefficient ($\geq 10^4$ cm^{-1}), suitable band gap (~1.5 eV) and non-toxicity. Because of these properties, CZTS is a promising semiconductor as a solar cell absorber layer. CZTS thin film based solar cell devices can be fabricated by simple sol-gel techniques. In this thesis, a CZTS based solar cell was fabricated by sol-gel spin coating method and the diode current was modeled. In the first part of the thesis, the effects of spin coating and subsequent heat treatment parameters on the properties of the films were investigated in terms of composition, grain size, surface morphology, crystallinity and film thickness. Another shortcoming in the literature is the study examining the dependence of the CZTS crystal phase formation on heat treatment. Therefore, the effects of annealing process on the crystallinity were investigated in detail. At the end of the first part, the effect of different annealing temperatures on nonlinear optical properties of CZTS thin films was investigated. In the second part of the thesis, CZTS-based p-n diode was fabricated and the current was modeled using only experimental data without the need for a computer. Diode ideality factor, saturation current and series-shunt resistor variables were successfully attained through the realistic diode equation.

Key Words: CZTS, thin film, spin coating, diode equation, analytic modeling.

ÖZ

DOKTORA TEZİ

SPIN COATED CZTS SOLAR CELLS AND ANALYTICAL MODELLING

Teoman ÖZDAL

ÇUKUROVA ÜNİVERSİTESİ
FEN BİLİMLERİ ENSTİTÜSÜ
FİZİK ANABİLİM DALI

Danışman : Prof. Dr. Hamide KAVAK
Yıl: 2020, Sayfa: 85
Juri : Prof. Dr. Hamide KAVAK
: Prof.Dr. Gülfeza KARDAŞ
: Doç. Dr. Mustafa GÜNEŞ
: Dr. Öğr. Üyesi Şadi YILMAZ
: Dr. Öğr. Üyesi Mehmet Ali OLĞAR

Fotoaktif bakır çinko kalay sülfür (Cu_2ZnSnS_4, CZTS) yarıiletkenler, düşük maliyetli, yüksek soğurma katsayısı ($\geq 10^4$ cm^{-1}), uygun bant aralığı (~ 1.5 eV) ve doğaya zararlı olmaması nedeniyle son yıllarda geniş çapta incelenmiştir. Bu özelliklerinden dolayı, CZTS, bir güneş pili soğurucu katmanı olarak gelecek vaat eden bir yarı iletkendir. CZTS ince film tabanlı güneş pili cihazları, basit sol-jel teknikleriyle üretilebilir. Bu tezde, CZTS tabanlı bir güneş pili, sol-jel spin kaplama yöntemi ile üretilmiş ve diyot akımı modellenmiştir. Tezin ilk bölümünde spin kaplama ve sonraki ısıl işlem parametrelerinin filmler üzerindeki etkileri kompozisyon, tanecik boyutu, yüzey morfolojisi, kristallik ve film kalınlığı açısından incelenmiştir. Literatürdeki bir diğer eksiklik ise CZTS kristal faz oluşumunun ısıl işleme bağımlılığını inceleyen çalışmadır. Bu nedenle tavlama işleminin kristallik üzerindeki etkileri detaylı olarak incelenmiştir. Birinci bölümün sonunda, farklı tavlama sıcaklıklarının CZTS ince filmlerin doğrusal olmayan optik özelliklerine etkisi araştırılmıştır. Tezin ikinci bölümünde, CZTS tabanlı p-n diyot üretilmiş ve akım, bilgisayara ihtiyaç duymadan sadece deneysel veriler kullanılarak modellenmiştir. Diyot ideallik faktörü, doyma akımı ve seri-şönt direnç değişkenleri, gerçekçi diyot denklemi ile başarıyla elde edilmiştir.

Key Words: CZTS, ince film, spin kaplama, diyot denklemi, analitik modelleme.

EXTENDED ABSTRACT

CZTS photoactive semiconductors have been widely studied recently due to the advantages of low-cost, absorption coefficient higher than 10^4 cm^{-1}, ~1.5 eV suitable band gap and non-toxicity. This promising kesterite semiconductor structure is the ideal solar cell absorber layer. CZTS semiconductors can also be fabricated using spin coating methods that do not require expensive high vacuum and complicated technologies. On the other hand, it is important to detail the various stages of the spin coating process. So far, a comprehensive parameter analysis about the growth of spin-coated CZTS absorbing layers has been lacking in the literature; therefore, here the effects of spin speed, solution molarity, amount of stabilizer, drying and subsequent annealing parameters on the films were investigated in terms of composition, grain size, surface morphology, crystallinity and film thickness. It has been found that the spin speed and molarity are effective on the film quality, but this effect is not sufficient. The quality of the prepared CZTS thin film is largely dependent on the heat treatment. Various drying, annealing temperatures and atmospheres were used and optimum heat treatment parameters obtained. As a result, spin coating and subsequent heat treatment parameters for the stoichiometric CZTS thin film absorber layer were determined. The effects of annealing temperature and time on the crystallization of CZTS thin film were investigated in terms of crystallinity, morphology, composition, and optical and electrical properties. The annealing process was achieved in a tube furnace under N_2 gas flow and S vapor. The importance of this work is the detailed investigation of annealing temperature and its effect on the CZTS thin films that were prepared by the sol-gel spin coating method. The threshold temperature where the film begins to crystallize has been determined to be 465 °C. A temperature increase of 15 °C from 450 to 465 °C boosted the crystallite size and main peak intensities and optimized energy gap from 1.38 to 1.46 eV. In summary, the effect of the annealing temperature on the crystallinity of the films was studied in detail and the threshold temperature value which improved the crystallinity was determined. The effect of different annealing temperatures (300, 400, 500 and 550 °C) on the nonlinear optical properties of CZTS thin films that were deposited on glass substrate employing a sol–gel spin-coating method was also investigated. The obtained results for X-ray diffraction (XRD) indicate a polycrystalline structure of CZTS thin film, the scanning electron microscopy (SEM) and atomic force microscopy (AFM) micrographs showed a uniform and dense texture of the

samples, besides the effect of annealing temperatures on CTZS morphology and surface was discussed. Linear optical properties of CZTS thin films were performed by UV–Vis spectrophotometer, both band-gap energy and absorption coefficient were determined and extracted from the variation of the optical transmission and absorption with the wavelength, Eg of the films annealed at 300, 500 and 550 °C was found to be 1.58 eV against 1.63 eV for the film annealed at 400 °C. However, the optical nonlinearity characterizations of CZTS films examined by third harmonic generation (THG) technique exhibited an interesting nonlinear optical response between 1.10E–20 and 1.84E–20 m^2 V^{-2} which can enlarge the application field of the studied material. Undesired phases that easily occur in the CZTS structure prevent approaching the theoretical limit. In addition, interface defects are another significant factor that decreases the solar cell device efficiency. It is important to identify these defects that degrade the performance of the device. Detailed analysis methods, on the other hand, are expensive and complex physical processes that mostly extend and limit the analysis process. The determination of some properties of the device through analytical modeling is an important convenience to indicate the structural defects. However, the complex methods used for modeling and calculation are usually performed with the help of computers. In the second part of thesis, CZTS-based p-n diode current was fabricated and modelled using only experimental data without the need for a computer. Diode ideality factor, saturation current and series-shunt resistor variables were successfully attained through the realistic diode equation. Structural and interfacial defects are tried to be explained through the variables.

GENİŞLETİLMİŞ ÖZET

CZTS fotoaktif yarı iletkenler, düşük maliyetli, 10^4 cm^{-1} değerinden yüksek soğurma katsayısı, ~ 1.5 eV değerinde uygun bant aralığı ve zehirli olmaması nedeniyle son zamanlarda geniş çapta incelenmiştir. Bu gelecek vaat eden kesterit yarı iletken yapı, ideal bir güneş pili soğurucu katmandır. CZTS yarı iletken ince filmler, pahalı, yüksek vakumlu ve karmaşık teknolojiler gerektirmeyen spin kaplama yöntemleri kullanılarak da üretilebilir. Öte yandan, spin kaplama ile üretim işleminin çeşitli aşamalarını detaylandırmak, aşamaları optimum verimlilikle tamamlamak önemlidir. Şimdiye kadar, spin kaplama ile CZTS soğurucu ince film katmanların büyütülmesi hakkında kapsamlı bir parametre analizi literatürde eksiktir; bu nedenle burada spin hızı, çözelti molaritesi, stabilizatör miktarı, kurutma ve sonraki ısıl işlem parametrelerinin filmler üzerindeki etkileri kompozisyon, tanecik boyutu, yüzey morfolojisi, kristallik ve film kalınlığı açısından incelenmiştir. Dönme hızı ve molaritenin film kalitesi üzerinde etkili olduğu bulunmuştur ancak bu parametreler daha iyi bir ince film üretmek için yeterli değildir. Üretilen CZTS ince filmin kalitesi büyük ölçüde ısıl işleme bağlıdır. Çalışmamızda öncelikle çeşitli kurutma ve tavlama sıcaklıkları kullanılarak ve üretimin yapıldığı atmosfer değiştirilerek optimum ısıl işlem parametreleri ve atmosfer koşulları elde edilmiştir. Sonuç olarak, stokiyometrik CZTS ince film soğurucu tabaka için spin kaplama ve takip eden ısıl işlem parametreleri belirlenmiştir. En son ısıl işlem olan tavlama sıcaklığının ve süresinin CZTS ince filmin kristalleşmesi üzerindeki etkileri kristallik, morfoloji, kompozisyon, optik ve elektriksel özellikler açısından ayrıca incelenmiştir. Tavlama işlemi, en uygun koşul olarak bulduğumuz N_2 ve S buharı altında bir tüp fırında gerçekleştirilmiştir. Bu çalışmanın önemi, tavlama sıcaklığının sol-jel spin kaplama yöntemiyle üretilen CZTS ince filmlerin kristalliği üzerindeki etkisinin detaylı bir araştırma olmasıdır. Çalışma sonunda filmin kristalleşmeye başladığı kritik sıcaklığın 465 °C olduğu belirlenmiştir. 450 °C 'den 465 °C'ye olan 15 °C'lik bir sıcaklık artışı, filmin kristalit boyutunu ve kristallik ana piklerin şiddetini

arttırmış, yasak bant aralığını 1,38 eV'den 1,46 eV'ye yükseltmiştir. Buraya kadar özetle, çözelti ve spin kaplama ile takip den kurutma ve tavlama ısıl işlemlerinin filmlerin kristalliği üzerindeki etkisi detaylı olarak incelenmiş ve filmin kristalliğini iyileştiren optimum parametreler belirlenmiştir. Bir diğer çalışmamızda farklı tavlama sıcaklıklarının (300, 400, 500 ve 550 °C), sol-jel spin kaplama yöntemi kullanılarak cam alttaban üzerine büyütülen CZTS ince filmlerin doğrusal olmayan optik özellikleri üzerindeki etkisi de araştırılmıştır. Bu çalışmada yapılan karakterizasyonlar, CZTS ince filmin polikristal yapısını, numunelerin homojen ve yoğun dokusunu göstermiştir. CTZS filmlerin morfolojisi ve sıcaklığın etkisine bağlı optik özellikleri tartışılmıştır. Dalga boyu ile optik iletim ve soğurma özelliklerinin değişiminden, numunelerin hem soğurma katsayısı hem de optik bant aralığı enerjisi belirlenmiştir. 300, 500 ve 550 °C'de tavlanan filmler için 1,58 eV, 400 ° C'de tavlanan film için ise 1,63 eV olarak bulunmuştur. Bununla birlikte, CZTS filmlerinin Üçüncü Harmonik Üretimi (THG) tekniği ile incelenen doğrusal olmayan optik karakteri, incelenen materyalin uygulama alanını genişletebilen, 1,10E–20 ile 1,84E–20 m^2 V^{-2} arasında ilginç bir doğrusal olmayan optik yanıt sergilemiştir. Diğer taraftan CZTS kristal yapısında kolaylıkla oluşan istenmeyen fazlar, bu yapının güneş pili uygulamalarındaki veriminin teorik olarak belirlenen veriminin sınırına yaklaşılmasını engeller. Ek olarak, güneş pili aygıt katmanları arayüzey hataları, güneş pili cihaz verimliliğini azaltan bir diğer önemli faktördür. CZTS ile üretilen güneş pili aygıtın verimini düşüren bu kusurların belirlenmesi ayrıca önemlidir. Bu yapısal ve arayüzeyler ile ilgili kusurların ayrıntılı fiziksel analiz yöntemleri ise, analiz sürecini çoğunlukla uzatan sınırlı, pahalı ve karmaşık süreçlerdir. Aygıtın özelliklerinin analitik modelleme yoluyla belirlenmesi, yapısal ve arayüzeysel kusurları belirtmek için önemli bir kolaylıktır. Ancak modelleme ve hesaplama için kullanılan karmaşık yöntemler genellikle bilgisayar yardımı ile gerçekleştirilir. Tezin ikinci bölümünde, CZTS tabanlı p-n diyot akımı, bilgisayara ihtiyaç duyulmadan sadece deneysel veriler kullanılarak yaklaşık olarak modellenmiştir. Diyot ideallik faktörü, doyma akımı ve seri-şönt direnç değişkenleri, gerçekçi diyot denklemi kullanılarak başarıyla elde edilmiştir. Yapısal ve arayüzey kusurları değişkenler aracılığıyla açıklanmaya çalışılmıştır.

ACKNOWLEDGEMENTS

I dedicate my dissertation work to my loving parents, Neziha and Mustafa Özdal. I also dedicate this thesis to Dönüş who supported me throughout the process. Thank you for believing in me, and for allowing me to further my studies. I would like to thank Prof. Dr. Gülfeza KARDAŞ and her team for their support. Besides my advisor, I would like to thank the rest of my thesis committee: Prof. Dr. Gülfeza Kardaş, Assoc. Prof. Dr. Mustafa GÜNEŞ, Asst. Prof. Dr. Şadi YILMAZ, and Asst. Prof. Dr. Mehmet Ali Olğar, for their encouragement, insightful comments, and hard questions. Last but not least I dedicate this work and give special thanks to my supervisor Hamide Kavak for helping me throughout the entire doctorate program.

CONTENTS **PAGE**

LIST OF TABLES **PAGE**

LIST OF FIGURES **PAGE**

ABREVIATONS

ε_0	: Permittivity of free space
I_0	: Diode saturation current
I_{DIFF}	: Diffusion current
I_{R-G}	: Thermal recombination-generation current
N_D	: Donor density
V_{bi}	: Built in potential in the depletion region
n_i	: Intrinsic carrier density
τ_n and τ_p	: Electron and hole minority-carrier lifetime
μ	: Mobility
D	: Crystallite size
D_{AV}	: Average crystallite size
h	: Planck constant
I	: Current
J	: Current density
K	: Temperature
k_B	: Boltzman constant
n	: Carrier concentration
n_0	: Refractive index
q	: Electron charge
R	: Reflectance
R_{diff}	: Differential resistance
T	: Transmittance
β	: Full width at half maximum
δ	: Dislocation density
ε	: Microstrain
θ	: Bragg diffraction angle

λ	: Wavelength
ρ	: Resistivity
$\chi^{(3)}$	: Third-order nonlinear optical susceptibilities
A	: Junction area
C	: Capacitance
W	: Depletion region width

1. INTRODUCTION

Due to the rapid spread of electronic devices in everyday life and the growing population, the need for electricity is increasing day by day. The greenest and most effective way of meeting this need is the use of solar cells, which generate electricity from an infinite source. Therefore, efficient solar cell devices consist of earth abundant and non-toxic materials are the key factors for clean energy needs of the future (Green, 2000, 2006). In this regard, CZTS kesterites are promising semiconductor materials for non-toxic solar cell devices (Liu et al., 2016; Guo et al., 2017). It provides an environmentally friendly and low-cost alternative to $CuIn_xGa_{1-x}Se_2$ (CIGS) and $CuInS_2$ (CIS) structures by including zinc (Zn) and tin (Sn) instead of indium (In) and gallium (Ga) elements (Bonazzi et al., 2003; Hall et al., 1978; Amiria et al., 2013; Amiria et al., 2014). An early study of the CZTS thin films as an absorber layer shows that p-CZTS semiconductor is highly suitable for solar cell applications with 1.45 eV direct optical energy band-gap (Ito and Nakazawa, 1988). But since the efficiencies of CIGS based solar cell devices are much higher, little progress has been made in CZTS based structures. The slow-paced studies on CZTS based solar cell devices accelerated after 2000's (Kumar et al., 2015; Song et al., 2014). Although the first samples were mostly fabricated by vacuum technology, subsequent growth of efficient CZTS absorber layers were mostly achieved by sol-gel methods (Wei et al., 2016; Dong et al., 2017; Awadallah and Cheng, 2017; Tao et al., 2017). Among the sol-gel methods, the spin coating is generally less costly, requires very simple preliminary preparation and is quite promising. Also, the highest efficiency solar cell devices with CZTS absorber layer are fabricated by the spin coating method (Sun et al., 2016). While there was no comprehensive parameter analysis for spin coated CZTS absorber layer growth in studies, we intended to complete the lack of extensive parameter analysis in the literature. Firstly, the effect of spin speed, solution molarity and composition parameters of the CZTS absorber layer were

investigated. The effect of the number of layers on the film thickness and crystallinity were also investigated. Finally, it was focused on the effects of drying, annealing temperature and atmosphere on the properties of CZTS absorber layer.

Although CZTS absorber layer studies advanced considerably over the last decade, it was not possible to increase its efficiency to reach the level of the CIGS alternative (Zhuk et al., 2017; Wang et al., 2014; Sun et al., 2016; Kato et al., 2017). The main reason for the low efficiency is the difficulty of fabricating single-phase CZTS absorber layer. In spite of its low-cost and easy producibility advantages, there are still unsolved problems relating to the crystal structures (Olekseyuk et al., 2004; Berg and Dale, 2014; Kumar et al., 2015). Given that the highest efficiency is obtained by spin coating (Wang et al., 2014; Sun et al., 2016), the effect of each step of the production process on crystallinity should be investigated in detail. Researchers should focus on two main steps that strongly determine the crystal quality: solution preparing and post-annealing heat treatments (Wei et al., 2016; Muska et al., 2011; Ge et al., 2012; Kunihiko et al., 2008). The post-annealing step relates entirely to the crystallinity of CZTS films. It completes the process of forming the ideal stoichiometry that determines the electrical and optical properties of the films. Although the most efficient CZTS based solar cell devices are produced with sol-gel spin coating method, there is still no detailed annealing temperature analysis for this technique. Moreover, the critical temperature value that significantly increases crystallinity has not been determined. A step by step annealing temperature analysis with respect to crystallinity, morphology, composition, optical and electrical features will help researchers to prepare efficient CZTS absorber layers. For this reason, we also aimed to investigate the effect of annealing temperature levels on the properties of sol-gel spin-coated CZTS thin film.

The investigations of the effect of different annealing temperatures on optoelectronics of thin film-based inorganics semiconductors are crucial for diverse optoelectronics applications (Fernandes et al., 2011; Schubert et al., 2011). Here

we extended the area of employment of CZTS to reach the nonlinear optical (NLO) applications based on the preliminary gotten results, specifically for the third order nonlinear optical responses. However, before we will reach this purpose, more analysis has to be accomplished. We present the experimental results concerning the examination of CZTS thin films by inspecting the impact of annealing temperature on the nonlinear optical properties of CZTS thin films.

CZTS-based solar cells have attracted intense attention as they are an alternative to CIGS structures, but this interest has decreased gradually because of the inability to approach theoretical efficiency. The major problem that negatively affects the efficiency is the difficulty of growing the CZTS crystal structure in the pure phase and the possible defects which significantly limit the photocurrent. Undesired binary and ternary compounds inside the CZTS layer create secondary phases and bulk defects which deteriorate the device performance (Kumar et al., 2015). Furthermore, possible irregularities of elemental states in the interface as a result of a non-ideal junction between CZTS and adjacent layer have also negative effects on the heterostructure properties (Park et al., 2018). The existence of undesired secondary phases can be achieved by X-Ray Diffraction (XRD), Raman and X-Ray Photoelectron Spectroscopy (XPS) measurements. Successful identification and etching of unwanted phases on the CZTS surface will improve the interface properties. For example, Wei and his team successfully analyzed the condition of undesired phases on the surface of as-grown and chemically etched CZTS samples with the Raman analysis method (Wei et al., 2016). Zhang and his team were conducted XPS measurement at different depths on the CZTS surface and found that there were no undesirable phases below the 50 nm of the surface (Zhang et al., 2019). However, the analysis methods mentioned so far require expensive and complex processes. An alternative to the methods is modeling the I-V output characteristic of the diode and therefore the current equation. Determining and comparing the variables in the equation will provide information about structural defects. If the variables and thus the current equation can be acquired

quickly, the researchers will be able to compare the variables with the ideal values and focus related structural defects. For this purpose, we worked on easy and fast modelling of the current equation of CZTS-based heterojunction with the assistance of the trial-error method using dark I-V characterization data. We made inferences about structural/interface defects that depend on the values of the variables.

2. LITERATURE REVIEW

Based on the low-cost thermal decomposition, the researchers synthesized CZTS thin film absorber layer by optimizing the annealing temperature. In their work, they primarily focused on production costs. Later, they optimized the depletion zone to increase the cell efficiency. For this purpose, they were fabricated a novel solar cell using low-dimensional CdS@CdS nano-arrays synthetized by aqueous solution method which increases the junction area. Therefore, their extremely low-cost CZTS-based inverted solar cell structure has increased carrier collection surface area (Chen et al., 2016).

Su et al. (2015) replaced an amount of Zn with Cd to overcome the limitations such as band gap adjustement and crystallinity of CZTS. They optimized the optical band gap and degreased the undesired phase structures in the CZCTS by variation of the Zn/Cd ratio. The existence of ZnS undesired phase was decreased and the grain sizes were improved. The new CZCTS-based solar cell device efficiency is enhanged significanly from 5.30% to 9.24%.

Researchers improved the CZTS layer thin film quality by depositing low-cost, environmentally-friendly molecular solution. They fabricated the CZTS thin film with the combination of molecular solution with hydrophilic nanoparticle ink. As a result, carbon-rich fine-grain layer removed and Mo/CZTS contact interface is improved. The solar cell device efficiency is reached 4.92%. (Wang et al., 2016).

Yu et al. (2014a, 2014b) developed sol-gel deposition of 1.2 μm kesterite CZTS layer without specific sulfurization. Sulphur concentration of the final film is ~48%. While the as-deposited thin films were poorly crystalline, the annealed films are well crystalline. The film was deposited in three separate deposition and annealing process; spin coating and annealing. Annealing steps were achieved under N_2 atmosphere using quartz tube. They also investigated the effects of spin speed of 1500, 2000 and 3000 rpm on the properties of CZTS thin films. They investigated the relation between the spin speed and film morphology; the film

deposited at 3000 rpm shows a more densely packed and less pinhole morphology than the films deposited at lower spin speeds. The solar cell fabricated using the CZTS film deposited at 3000 rpm has shown a power conversion efficiency of 1.9%.

Researchers investigated the effect of annealing temperature of CZTS thin films with a rapid thermal treatment. The duration of preheating and sulfurization of spin coated film was increased from 10 min to 1 h. The investigation of the effect on the films were achieved by sulfurization from 350 to 600 °C for 1 h. By increasing the aneealing temperature under $H_2S + N_2$, the grain size of the films is increased and Cu_xS undesired phase formation is decreased. They found that the films sulfurized at temperatures higher than 400 °C sufficiently absorbed sulfur (Kazuya et al., 2011).

Park et al. (2013) developed non-toxic and simple non-aqueous sol–gel process with heat treatment under N_2 without sulfurization by resolving the evaporation problem of S and undesired phase formation. The film annealed at 540 °C exhibited a kesterite polycrystalline phase on a SLG substrate. They were successfully deposited Cu-poor and Zn-rich CZTS thin films with large grains and fewer grain boundaries.

Researchers were synthesized CZTS thin films by environmentally friendly technique using 1,3-dimethyl-2-imadazolidinone as a solvent for the preparation of highly viscous, homogeneous, nontoxic CZTS for the ink that eliminates the need for the use of additional binders or additives to disperse the precursors and N_2, S powder and H_2S annealing atmospheres. CZTS prepared using the ink has grain sizes are greater than 0.7 μm and with no detectable presence of carbon at the Mo/CZTS interface. An efficiency of the device fabricated with the CZTS layer is 5.67%. The CZTS annealed under different atmospheres has large densely packed grains without pin holes. The efficiency of the solar cell device fabricated using the CZTS annealed under air is 0.77% (Agawane et al., 2015; Tunuguntla et al., 2015).

Ganguly et al. (2017) studied the effect of hydrostatic pressure and temperature on electro-optic effect profiles and third-order nonlinear optical susceptibility of impurity doped GaAs quantum dots. The sample has been subjected to a polarized monochromatic electromagnetic field. They have found that varying the temperature and pressure often causes shift of the peaks of above NLO properties and also increase/decrease the peak heights when the sample is subjected to a polarized monochromatic electromagnetic field. All changes subtly depend on mode of application of noise in tuning above NLO properties of sample.

Researchers investigated the effect of the post thermal treatment of sol-gel dip coated ZnO thin films by photoluminescence measurement which was performed in a wide temperature range from 13 K to 300 K to measure the recombination lifetimes for both: as-deposited and the annealed samples. Second and third order nonlinear susceptibilities of the ZnO were found to be high enough for the potential applications in the optical switching devices based on refractive index changes (Zawadzka et al., 2014).

In this study, the CZTS based solar cell device; both the p-CZTS layer and the n-type layers grown on it were fabricated by the completely sol-gel method and the diode parameters were extracted from the dark current. Spin coating parameters of CZTS layer have been optimized and structural properties such as crystal phase purity and interface properties of the diode device have been investigated through the extracted parameters.

3. EXPERIMENTAL PROCEDURES

3.1. Preparation of CZTS absorber layer

In order to control and understand all solution preparation and spin coating processes, we aimed primarily to focus on the pioneering works in CZTS absorber layer production. The CZTS layers were prepared by the sol-gel method and the initial solutions were obtained by dissolving the metal salts in glycol ether (Fig. 3.1 and Fig. 3.2). The layers were spin coated on soda lime glass substrates which were cut (2.5 × 2.5 cm) and cleaned with acetone, ethanol and distilled water, respectively. $CuCl_2$, $SnCl_2$ and $ZnCl_2$ metal salt precursor chemicals were dissolved in 2-methoxyethanol (2-metho) and monoethanolamine (MEA) mixture. The sulfur (S) content in the CZTS final films was obtained by the sol-gel method without the use of hydrogen sulfide (H_2S) atmosphere at the annealing step.

Figure 3.1. CZTS precursor solution, spin coater and CZTS thin film on Mo substrate.

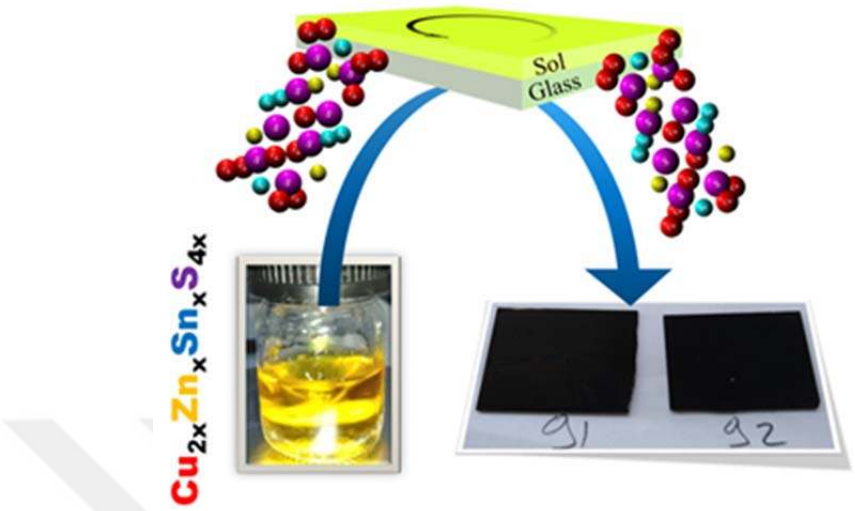

Figure 3.2. Schematic presentation of spin coating and following drying process of CZTS thin films.

In order to be able to compare the effects of the annealing atmosphere, some samples were annealed in N_2 with powdered S vapor. The ratio of the Cu, Sn, Zn and thiourea (S source) precursor chemicals in all prepared solutions was fixed at 2:1:1:8 (Tanaka et al., 2009; Yeh et al., 2009). The solutions were spin coated on the clean substrates for 60 s at different speeds of 1500, 2000, 2500 and 3000 rpm to investigate the effect of spin speed. Besides that, another sample was prepared twice as thick to study the effect of the number of coatings on the film thickness. Different solutions with various densities were prepared to analyze the molarity-film property relationship. For this purpose, four different solutions were prepared and spin coated: 1/2 M, 1/3 M and 1/4 M solutions were prepared by reducing the weight of chemicals initially calculated for 1 M Cu_2ZnSnS_4 by the ratio of 1/2, 1/3 and 1/4, respectively. The samples were deposited at the same speed to analyze the effects of the amount of. In addition, the amount of MEA on the film was also examined by changing the MEA ratio in the solution. All the deposition processes were followed by a drying stage which helps to evaporate solvent and stabilizer residues. The spin coated films were dried on a hot plate at different temperatures

of 165 and 300 °C to study the effect on the film properties. Spin coating and drying processes were repeated three times to obtain sufficient film thickness even if they were spin coated at various speeds from different solutions and drying temperatures. All the spin coated and dried films were annealed at 300, 350, 400, 450, 500 and 550 °C in air, N_2 and N_2 + S vapor for 30 min to examine the effects of annealing temperature and atmosphere on the film structures. Investigated parameters and their values according to analysis order are listed in Table 3.1. Unless otherwise noted, the samples prepared for comprehensive parameter analysis of spin coating and subsequent heat treatment process were spin coated three times at 3000 rpm and then dried at 165 °C and annealed at 300 °C in air.

Table 3.1. Investigated parameters and their values according to analysis order.

Parameters	Values					
Spin speed (rpm)	1500		2000	2500		3000
Film thickness	3 layers			6 layers		
Precursor rate	1/4		1/3	1/2		1
Stabilizer amount	1			1/6		
Drying temp. (°C)	165			300		
Annealing temp. (°C)	300	350	400	450	500	550
Annealing atmosphere	Air		N_2			N_2 + S

For the determination of crystallization threshold temperature, spin coating process was performed by spinning the substrates at 3000 rpm for 60 s. Spin coated samples were dried on a hot plate at 300 °C for 5 min to evaporate residues. The spin coating and drying processes were repeated three times to obtain sufficient film thickness. Samples were then annealed at temperatures ranging from 300 to 580 °C in N_2 + S vapor for 30 min to examine the effects of annealing temperature

on the film structures. All annealing processes were performed under high-purity N_2 gas flow (1.5 L/min) and 0.25g S powder vapor in a tube furnace.

Elaboration of annealing effects on the linear and nonlinear optical properties, samples were prepared by spin-coated on the substrates at 3000 rpm for 30 s and then dried at 300 °C for 5 min in air. The process was repeated three times to get the initial films with a desired thickness. The process was accomplished by annealing CZTS thin film layers in the combination of high-purity N_2 and S environment for 30 min in a tube furnace at 300, 400, 500 and 550 °C. The final film was acquired at 2:1:1:4 elemental ratio for Cu:Zn:Sn:S.

The analyzes so far have been discussed in section **4**, and the optimum parameters have been determined.

3.2. Device fabrication

For I-V characterization, Mo/CZTS/CdS/ZnO device structure was fabricated. Copper, zinc, tin and sulfur precursors solution was spin coated on Mo/glass substrates and then sulfurized under a combination of N_2 + S vapor. CZTS surface etching process was achieved via dipping the films in aqueous KCN (5wt%) solution for 120 s (Bär et al., 2011). CdS and ZnO thin film layers were deposited using CBD and spin coating method, respectively. Cadmium sulfate (0.003 M) and thiourea (0.03 M) dissolved in pure water under vigorous stirring. Ammonia (25%) (1.6 M) was then added slowly to the sol and heated up to 70 °C. The CZTS film was dipped to the sol for 10 min (Fig. 3.3). After the deposition, CZTS/CdS film rinsed with pure water and annealed at 200 °C for 10 min. Zinc acetate salt and MEA stabilizer (1:1) were dissolved in isopropyl alcohol (or 2-metho) and then stirred for 2 h to obtain a transparent solution. The solution was then aged for 12 h before the spin coating processes. ZnO thin films were spin coated at 1500 rpm for 30 s (Fig. 3.4). The fabricated CZTS/ZnO and CZTS/CdS/ZnO heterojunction structures were annealed at 450 and 200 °C for 60 min, respectively. All front and back ohmic contacts were made using Ag paste.

The details of the heterojunction devices are listed in Table 3.2. The electrical characterization of the fabricated devices were performed employing solar simulator (Abet Technologies) under 100 mW/cm^2 (AM1.5) illumination.

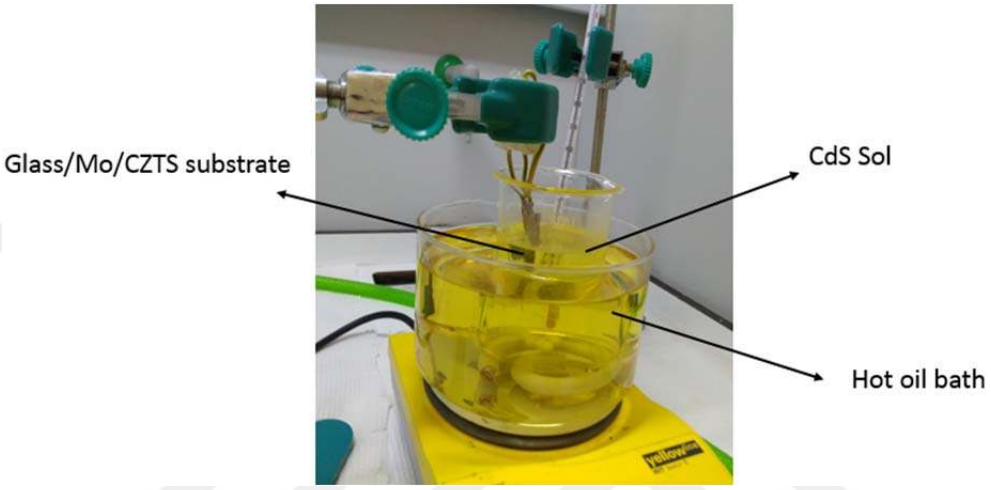

Figure 3.3. CBD deposition of CdS thin film onto Mo/CZTS substrate.

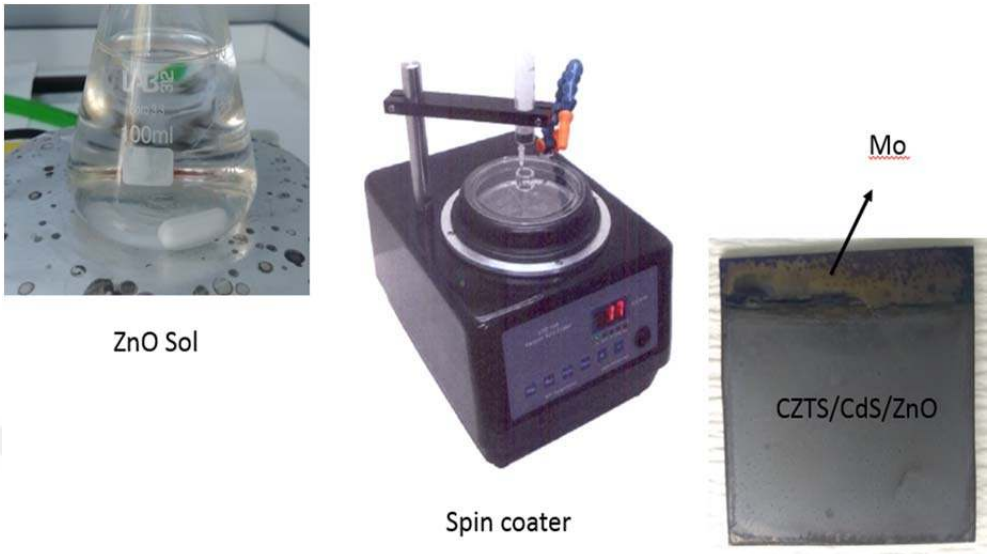

Figure 3.4. ZnO precursor solution, spin coater and Mo/CZTS/CdS/ZnO heterostructure.

Table 3.2. Fabricated CZTS-based heterojunction devices and processing details.

	Structure	KCN Treatment	ZnO Thickness (nm)	ZnO Solvent	ZnO Annealing (°C)
S1	CZTS/ZnO	×	300	2-propanol	450
S2	CZTS/ZnO	✓	300	2-propanol	450
S3	CZTS/ZnO	✓	600	2-propanol	450
S4	CZTS/ZnO	✓	300	2-metho	450
S5	CZTS/ZnO	✓	300	2-metho	200
S6	CZTS/CdS/ZnO	✓	300	2-metho	200
S7	CZTS/CdS/ZnO	✓	80	2-metho	200

3.3. Measurement techniques

The crystallinity of CZTS thin films were examined by XRD measurements (Rigaku Miniflex). Field Emission Scanning Electron Microscopy (FE-SEM) and energy-dispersive X-ray spectroscopy (EDX) characterizations (Zeiss Supra 55 and FEI Quanta FEG 650) were performed to determine surface/cross-section morphologies and elemental analysis of the films. The optical properties of the films were investigated by a double beam computer-controlled spectrophotometer (Perkin Elmer Lambda 2S) in the UV/VIS/NIR regions. The electrical properties of the films were determined by Hall Effect Measurement (Ecopia, HMS-3000) system using the four-probe van der Pauw technique with silver paste contacts on square cut films. Raman scattering spectra were performed using Renishaw inVia Raman microscope system with a 785 nm and 532 nm excitation wavelength laser. In the transmission scheme for S polarized fundamental laser beam, the measurements of the Third Harmonic Generation (THG) responses of studied films were carried out using the rotational Maker fringe technique in MOLTECH-Anjou Laboratory.

4. RESULTS AND DISCUSSION

4.1. Comprehensive analysis results

4.1.1. Spin speed analysis

The surface morphologies and thicknesses of the first set of thin films was spin coated using 1/2M solution at different coating speeds are shown in the inset FE-SEM images of Fig. 4.1 with respect to the spin speed. At lower speeds, denser and thicker, at higher speeds less dense, rougher and thinner films obtained as seen in the inset images (a-d). Surface images also show that the number and size of the pin holes increase directly with the coating speed. More material was lost and film thickness decreased at higher speeds. However, in some studies of the literature, researchers have achieved similar and different results as well (Yu et al., 2014; Islam et al., 2015; Majula et al., 2015). The speed-dependent material loss and crystallinity relationship with spin speeds is also inversely proportional, as expected. According to inset images and XRD patterns in Fig. 4.1, the film thickness decreased from 650 nm to 200 nm and the intensity of main CZTS peaks of (112), (220) and (312) planes (JCPDS 26-0575) decrease as the coating speeds increase. These main peaks disappear in films that are deposited at 3500 rpm and higher spin speeds. However, despite this decrease, the spin speed was selected as 3000 rpm in the subsequent sections with reference to the pioneering work in this area (Tanaka et al., 2009); the best granulated and crack-free film was obtained at 3000 rpm, and the homogeneity of the films disappeared at 3500 and higher rpm.

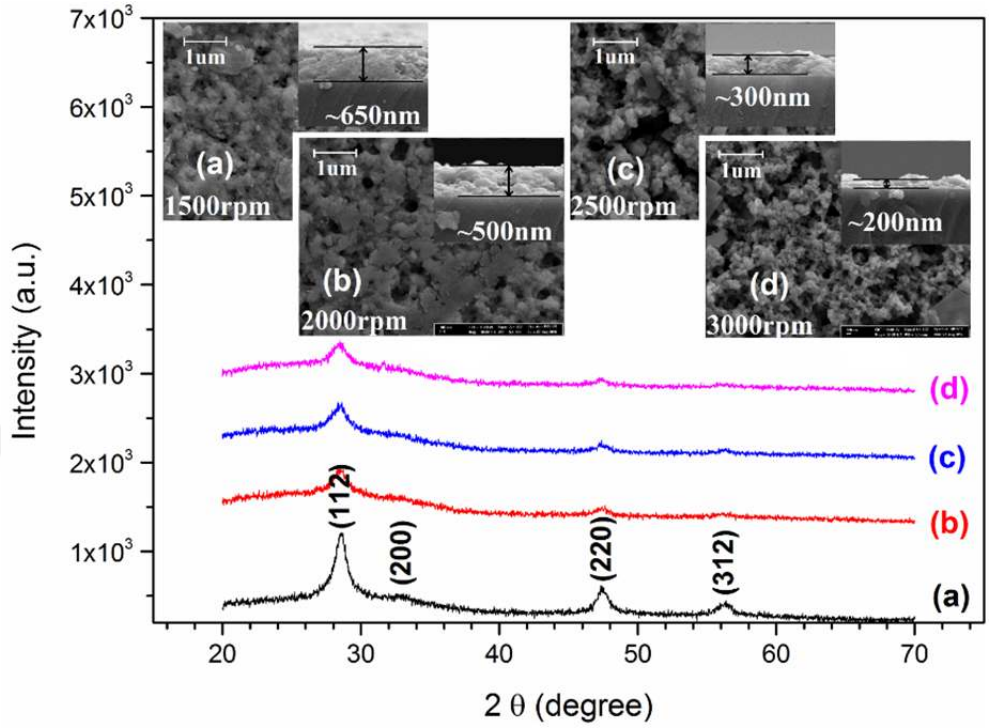

Figure 4.1. XRD patterns and surface/cross-section FE-SEM inset images of the films prepared at different spin speeds. As the coating speed increased from (a) 1500 rpm to (d) 3000 rpm, the main CZTS peak intensities and the thicknesses of the films decreased.

In order to confirm the film thickness-crystallinity relationship, two different samples were prepared at different thicknesses with 1 M solution and the results are presented in Fig. 4.2. The molarity was fixed to 1 M to allow for a more accurate thickness comparison. When the number of spin-coated layers, thus the film thickness doubled, the intensity of the main XRD peaks also increased, as shown in the plots of Fig. 4.2b.

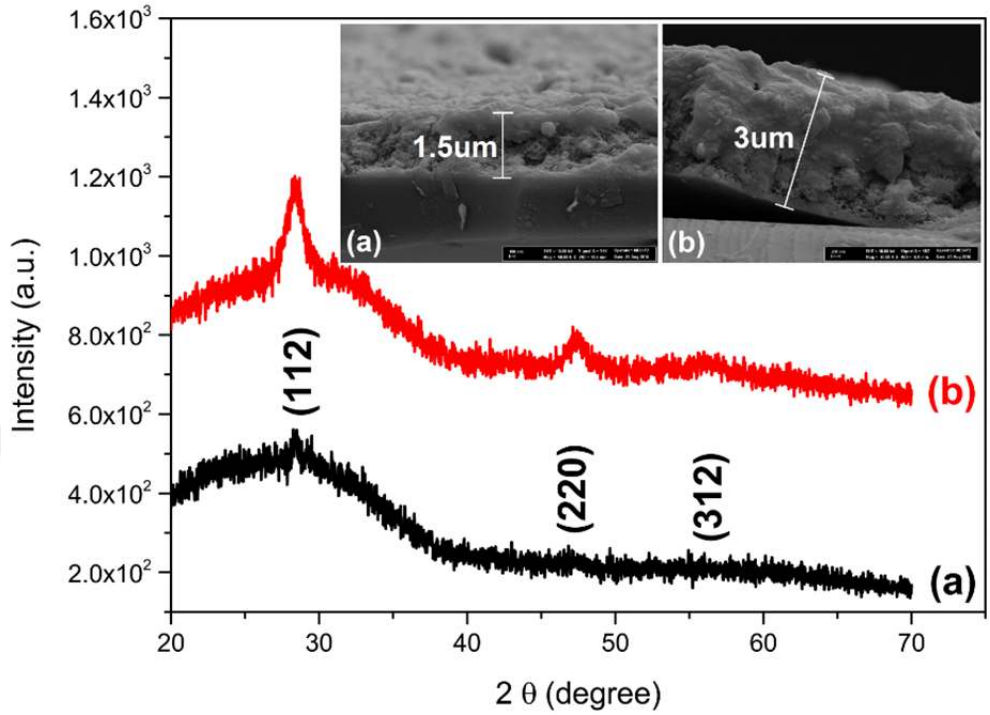

Figure 4.2. The intensities of main XRD peaks depending on film thickness. Film thickness doubles from (a) three layers to (b) six layers and the main peaks also increase.

4.1.2. Molarity dependent analysis

Four different solutions were prepared at various weight rates in the solution to investigate the effect on the crystal structure of the films. All spin coated samples with different precursor rate were dried and annealed. The effect of the precursor amount in the solution on grain size and hence on crystallinity was just as predicted. Better crystallinity was obtained for the sample shown in the inset XRD pattern of Fig. 4.3a with the largest grain size of 1 μm which is consistent with the literature and also supported by FE-SEM surface inset images of the films (Tanaka et al., 2011; Yeh et al., 2016). The scales of the x and y axes in the inset XRD plots are fitted together so that the curves can be compared. It is clear that the grain size for the film prepared with denser solution (1 M) is larger since all of the four films were prepared by the solutions with the same stoichiometry. As can be

seen from the inset images of a, b and c in Fig. 4.3, as the precursor rate decreases, the grain sizes decreased to approximately 1, 0.1 and 0.05 μm, respectively. When the rate is reduced to 1/4, very small grains combine to form clusters and size of these particle-like clusters are measured as 0.5 μm. The small increase in crystallinity may be due to these clusters. Inset image b also shows that cracks and only a few sheet-like structures were observed in the film prepared with the solution containing 1/2 precursor, these cracks and sheet-like structures disappeared when the 1/3 ratio solution was used. Large spaces are formed at the surface of the film for 1/4 ratio solution while the grains were formed as clusters of 0.5 μm in inset image d. An important detail was that immediately after the preparation of the 1/4 ratio solution, its clear yellow color turned into a dark greyish, and the spin-coated films with this solution were always dark grey before and after drying. That is, when the precursor rate is reduced to 1/4, the crystallization has started in solution as soon as it was prepared. Stoichiometric analysis was performed for the films prepared using 1, 1/2, 1/3 and 1/4 rate solutions. Cu/(Zn+Sn) ratio increased from 1.09 to 1.29 while the precursor rate decreased. Since the amount of Sn and S in the final film decreased due to evaporation despite annealing at 300 °C, the Zn/Sn ratio increased steadily as expected. This can be interpreted as the increase in the evaporation of Sn and S with decreasing the precursor rate. The best stoichiometry was obtained using 1 M solution and the results were consistent with the grain size and crystallinity of the films as discussed previously.

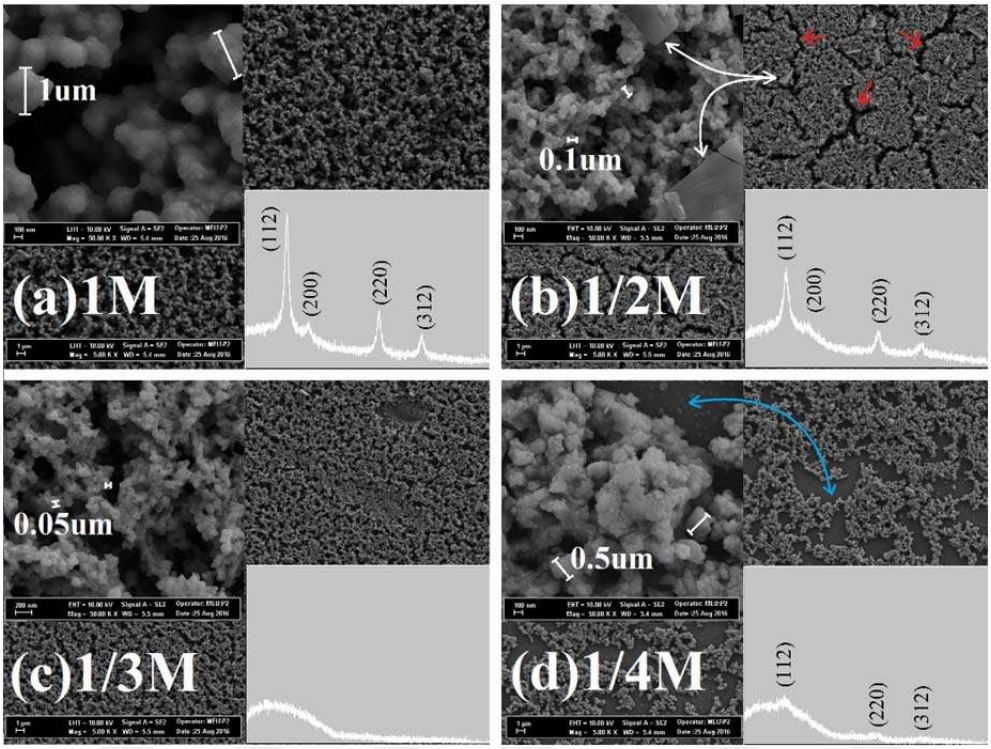

Figure 4.3. Surface FE-SEM images and inset XRD patterns of the films deposited with (a) 1, (b) 1/2, (c)1/3 and (d) 1/4 rate solutions. The grain size and hence the crystallinity is reduced due to the decrease in precursor rate. The scales of the x and y axes in the inset XRD plots are fitted together so that the curves can be compared.

4.1.3. Drying temperature analysis

One of the most challenging steps in the growth of semiconductor thin films by wet processes is to eliminate the detrimental effects of solvent residues on the resulting films. If the films are deposited by two or more layers, the complete elimination of solvent residues becomes even more crucial. The removal of residues from the resulting wet inorganic thin film structure is generally carried out by heat treatment. Two different drying temperatures of 165 and 300 °C were employed to evaporate the solvents in the wet coated films. First sample was dried at least at 165 °C, taking into account the evaporation temperature of the solvent (2-metho) and the humidity in the environment (air). Although the evaporation

temperature of the 2-metho was 125 °C, there was no blackening or significant color change in the film between the drying temperatures of 125-160 °C. As the drying temperature increased from 165 °C to 300 °C, the films dried quicker and they became darker in appearance. At temperatures above 300 °C, the films became more porous due to very rapid evaporation. This problem can be solved by gradually increasing the drying temperature but it takes more time. Previously, in a similar study, the same drying temperatures were used in order to eliminate different problems (Tanaka et al., 2008). In our study, max drying temperature was choosen as 300 °C, which is the lowest temperature at which the elements become compound when heated in air without any deterioration in the film structure. Therefore, the lowest 165 °C and highest 300 °C drying temperatures were applied for a clear analysis. XRD patterns in Fig. 4.4a and b show that the crystallinity of the film dried at 300 °C was more prominent than the film dried at 165 °C. The crystallinity of the CZTS thin film reveal that the optimal drying temperatures after the coating were about 300-350 °C, because the first layer which partially crystallized behaves as a guide layer for the second and subsequent layers (Maeda et al., 2011; Swami et al., 2013). In other words, the improvement in the crystallinity of the film dried at 300 °C is directly related to the increase in grain size as seen in the inset FE-SEM image b in Fig 4.4. The unexpected result after annealing was that the color of the film dried at 300 °C was lighter than the film dried at 165 °C. Stoichiometric analysis of the films shows that Sn and S losses in the film dried at 300 °C are higher and the film color shifts from black to a lighter tone which indicates an increase in the Cu ratio (Cu/metals) in the final film. The Zn/Sn ratio is 3.93 and the S/metal ratio is 0.33 for this film. These EDX results for the film dried at 300 °C deviate from the corresponding value for the films dried at 165 °C.

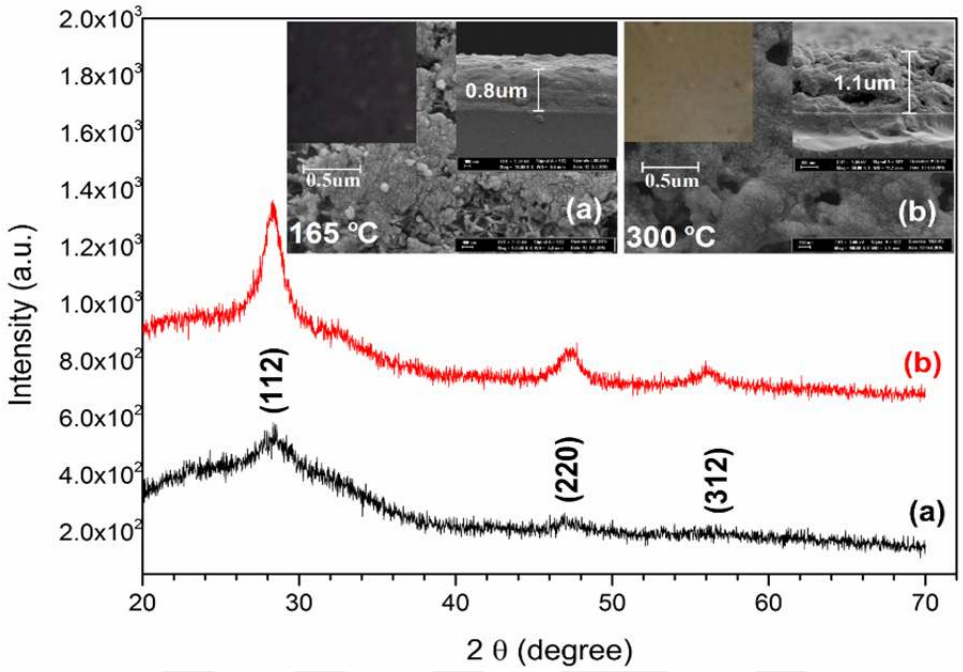

Figure 4.4. Surface/cross-section FE-SEM inset images, colour views and XRD patterns of the films dried at (a) 165 °C and (b) 300 °C. The film dried at 300 °C has larger grains and better crystallinity.

4.1.4. Annealing temperature analysis

All the samples were spin coated with 3000 rpm using 1 M solution then dried at 165 °C. Spin coating and drying process repeated three times, and subsequent annealing were carried out in air. The effect of annealing temperature was examined by surface and cross-section FE-SEM images and XRD patterns. As the annealing temperature increases, due to the increase of the grain sizes and sheet-like structures, the roughness also increases and the cracks are expected to disappear (Feng et al., 2017; Hergert and Hock, 2007; Shiyani et al., 2016). As the temperature increased more material has disappeared more than expected and the film colour gradually turned from black to red. Systematic decrease in the thickness as shown in Fig. 4.5, indicates the material loss due to the increased temperature. This undesired material loss and associated colour change are thought to be due to annealing of the films in air, and subsequent experiments support this

argument. When the effects of annealing temperatures on the stoichiometry were examined, Zn/Sn and Cu/(Zn+Sn) ratios increased due to Sn and S loss as the same of drying temperature analysis. Therefore, the S/metal ratio in the final films gradually decreased from 0.45 to 0.31 as the annealing temperature increased. The colours of the films have shifted from black to red due to the increase of the Cu/metal ratio.

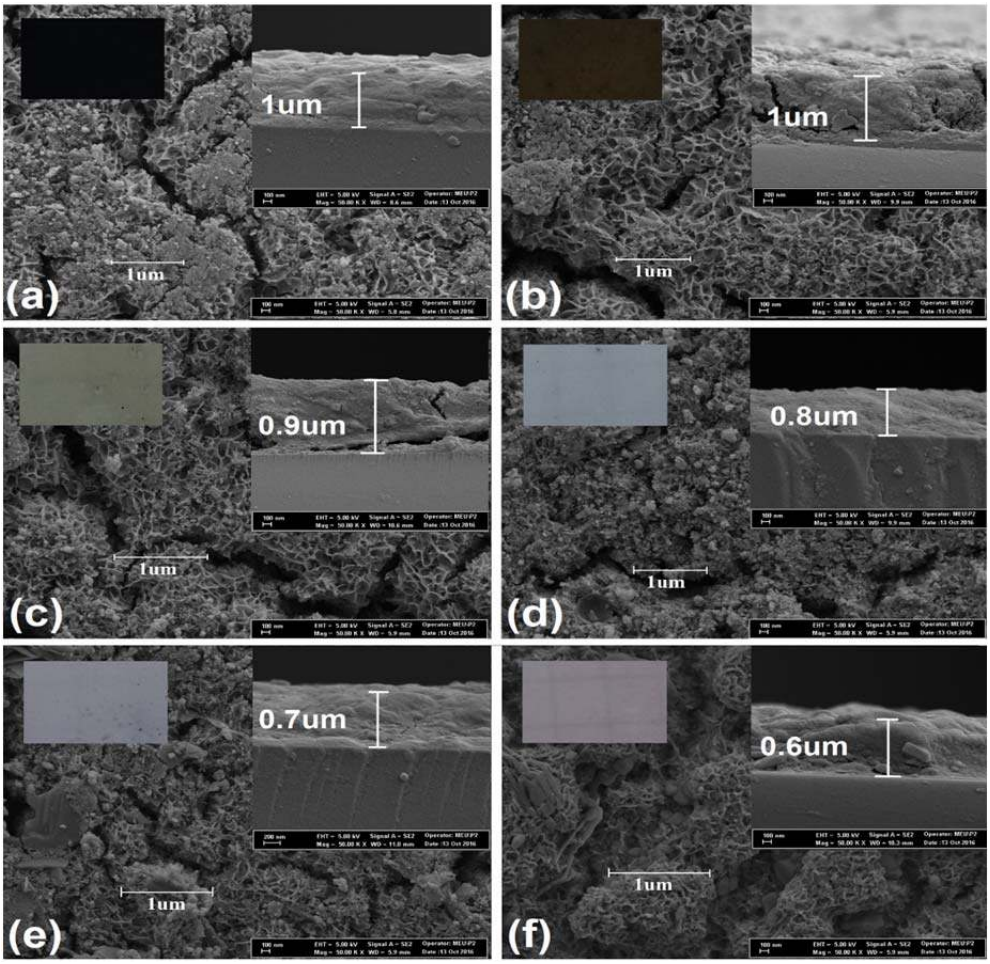

Figure 4.5. Surface and inset cross-section FE-SEM images of the films annealed at (a) 300 °C, (b) 350 °C, (c) 400 °C, (d) 450 °C, (e) 500 °C and (f) 550 °C in air. Cross-section and inset color images show that as the temperature increases, the thickness of the films decreases and the color of the films shifts to red.

4.1.5. Stabilizer quantity analysis

1 M solution was spin coated three layers at a speed of 3000 rpm and the drying temperature was set at 300 °C to ensure that all of the 2-metho and MEA residues completely evaporated. Two different solutions with various amounts of MEA were compared in order to investigate the effect of the decrease in the amount of stabilizer. Therefore, the amount of MEA in the second solution was set to 1/6 of the previous value to make a more reliable analysis. The film thickness is the same for both samples as shown in Fig. 4.6, however, surface morphology and crystallinity was different. FE-SEM image shows two important issues related to MEA-reduced film; film surface is cracked and no granulation occurred. It is clear that the film is not stoichiometric and the crystal structure is not suitable for an absorber layer, as investigated both experimentally and theoretically (Tanaka et al., 2010; Walsh et al., 2011). Indeed, as seen in the inset XRD patterns which the scales of the x and y axes are fitted together so that the curves can be compared, the CZTS main peaks of both films are almost identical, but an undesired CuS phase peak which signed as # appears as the MEA ratio decreased. This deterioration in film morphology due to the decrease in the amount of MEA used to prevent precipitation and reduce the effect of excessive amounts of thiourea has been observed as expected (Kim et al., 2012; Li et al., 2014; Part et al., 2014).

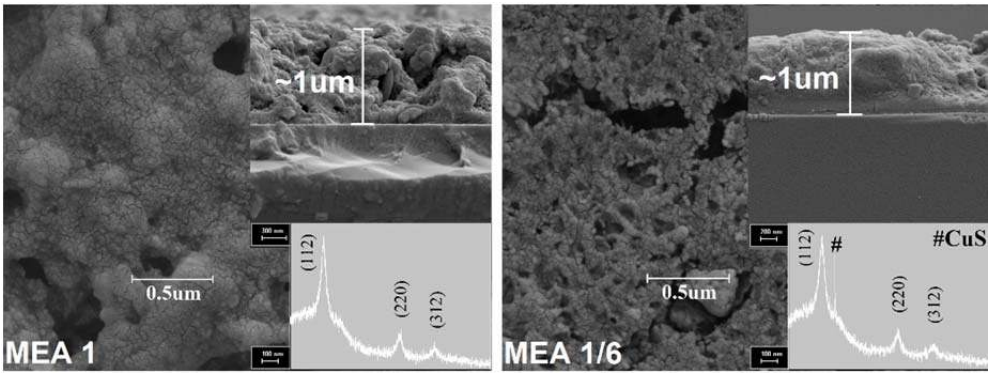

Figure 4.6. Surface and inset cross-section FE-SEM images and XRD patterns of the films prepared with 1 and 1/6 MEA. The surface morphology and grain size are different for both films. XRD pattern shows undesired CuS phase peak appears in the film as the MEA ratio decreased. The scales of the x and y axes in the inset XRD plots are fitted together so that the curves can be compared.

4.1.6. Annealing atmosphere analysis

Drying and annealing temperatures of the investigated CZTS thin films were set to 300 and 550 °C, respectively. The drying process was carried out in air for all three samples but the annealing process was carried out in air for sample (a), N_2 for sample (b) and N_2 + S vapor for sample (c) of Fig. 4.7. As can be seen from the FE-SEM images, there was a big difference between the samples annealed in air and N_2 ambient in terms of surface morphology and grain sizes. Grain size and crystallinity greatly improved for the sample annealed in N_2. In addition, material loss due to evaporation of the film was reduced and the film thickness increased to about 2.3 μm (Teeter et al., 2010; Weber et al., 2010). As can be seen from the inset color view of the film annealed in air (Fig. 4.7a), the color of the film is shifted to red due to the loss of Sn and S, other than Zn and Cu. Similar results were obtained and discussed for the films annealed at different temperatures above. As a result of the annealing process in N_2, the loss of the materials by evaporation is partially prevented and the structure of the CZTS compound is preserved, which leads to a tremendous improvement in the crystal structure. However, despite the

improvement in the structure, still there are undesired SnS and $C_{39}S_{28}$ (indicated by the "+" sign in the XRD pattern in Fig. 4.7) phases present in the composition (Khalkar et al., 2013; Yin and Gong, 2012), although their intensity is very low compared to the main CZTS peaks. In order to compensate for the loss of the element of S via evaporation, S powder was added to the annealing chamber. As a result of sulfurization, main CZTS peaks of the film were further increased, SnS and other undesired phase disappeared, but this time Cu_3SnS_4 phase marked with * at $2\theta = 31.7°$ appeared (Bouaziz et al., 2007; Chalapathi et al., 2014; Fernandes et al., 2010; Lin et al., 2012) and this new undesired phase is discussed with Raman measurement below. Sulfurization also reduced the evaporation of the materials and the film thickness of ~3.8 μm was obtained. So far, the greatest improvement in stoichiometry was achieved by annealing the samples in N_2. While extra carbon and oxygen elements were found in the chemical structure of the sample annealed in air, the elemental carbon disappeared and the amount of elemental oxygen was considerably reduced in the sample annealed in N_2. The final optimization of the annealing process was achieved by sulfurization of the sample in the N_2 and S vapor, thus completely eliminating the elemental oxygen as can be seen from the field EDX plot in Fig. 4.8. The plot shows that elemental oxygen in the sulfurized film completely disappeared, the amount of S, Zn and Cu increased and a substantial improvement in the stoichiometry was achieved. Table 4.1 quantitatively lists the elemental variation of the annealed films in the air, N_2 and N_2 + S. Due to the evaporation of Sn and S during the annealing at higher temperatures under uncontrolled atmospheric conditions, i.e. air, the stoichiometry of the film hence the crystal structure of CZTS is distorted. The carbon element disappeared by annealing in N_2, but the oxygen element was not completely eliminated. By saturating the annealing atmosphere with S vapor, stoichiometry of the film was preserved since the high temperature evaporation losses of SnS are completely prevented (Paire et al., 2014). Raman scattering spectroscopy was performed to further identify the phases. The effect of annealing atmosphere on the

phase structure is also confirmed by Raman scattering measurements as shown in Fig. 4.9. Tetragonal Cu_2SnS_3 (297.93 cm^{-1}) phase which formed due to high material loss and deterioration of the stoichiometry was predominant in the sample annealed in air (Cheng et al., 2011; Ghediya et al., 2016). This undesired phase is eliminated and only CZTS phase was observed in the film annealed in N_2. The two dominant CZTS Raman peaks at 337.51 cm^{-1} and 287.67 cm^{-1} show a major improvement in the crystal structure of this film (Dimitrievska et al., 2014a, 2014b; Guc et al., 2016). Raman peaks of sulfurized and N_2 annealed films coincide with the XRD results as expected. The undesired Cu_3SnS_4 phase peak at 320.95 cm^{-1} was appeared again. This phase is probably the result of the coupling of CuS binary phase, which is formed due to excess sulfurization, with Cu_2SnS_3 ternary phase (Chen et al., 2017; Khalil et al., 2015; Nguyen et al., 2015) and may be eliminated by reducing the initial rate of thiourea precursor. In addition, Cu:Zn:Sn:S ratio of the film obtained after the sulfurization is approximately 2:1:1:4 as in the case of solution preparation and this ratio can also be seen in Table 4.1.

Table 4.1. Stoichiometry of the films annealed in air, N_2 and N_2 + S vapor.

	Atomic %								
	O	C	S	Sn	Cu	Zn	Cu/(Zn+Sn)	Zn/Sn	S/metals
Air	54.87	3.08	10.88	2.97	13.19	15.01	0.73	5.05	0.34
N_2	37.04	—	30.95	9.55	16.26	6.20	1.03	0.64	0.96
N_2+S	—	—	51.77	10.87	25.10	12.26	1.08	1.12	1.07

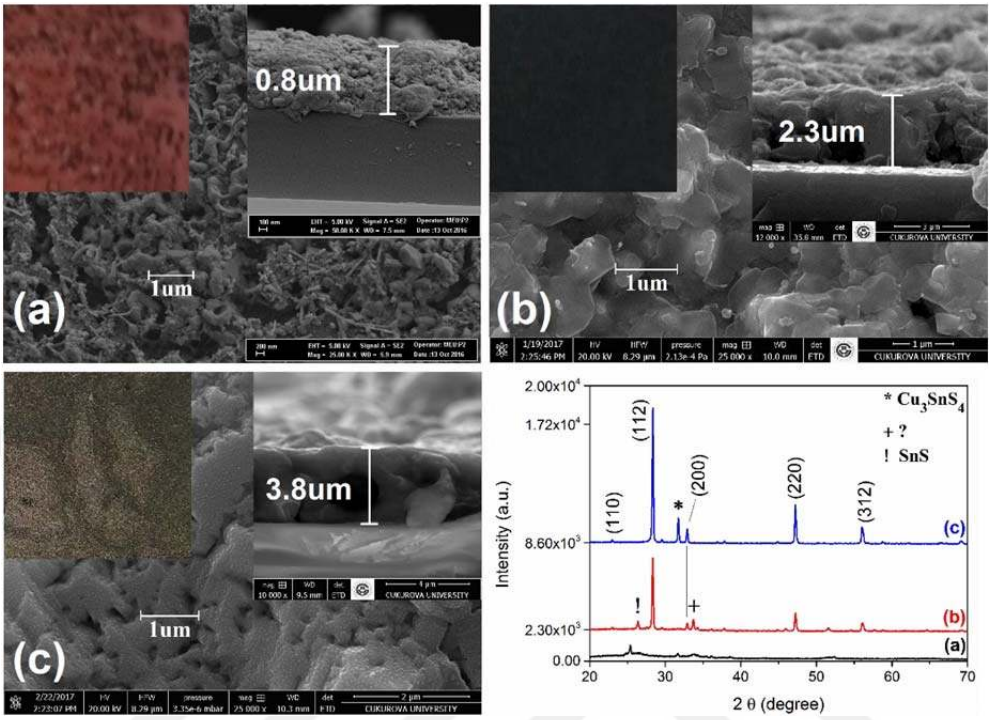

Figure 4.7. Surface and inset cross-section FE-SEM and color images of the films annealed in (a) air, (b) N_2 and (c) N_2 + S vapor. XRD patterns show that the main CZTS peak intensities for the sulfurized film increased significantly.

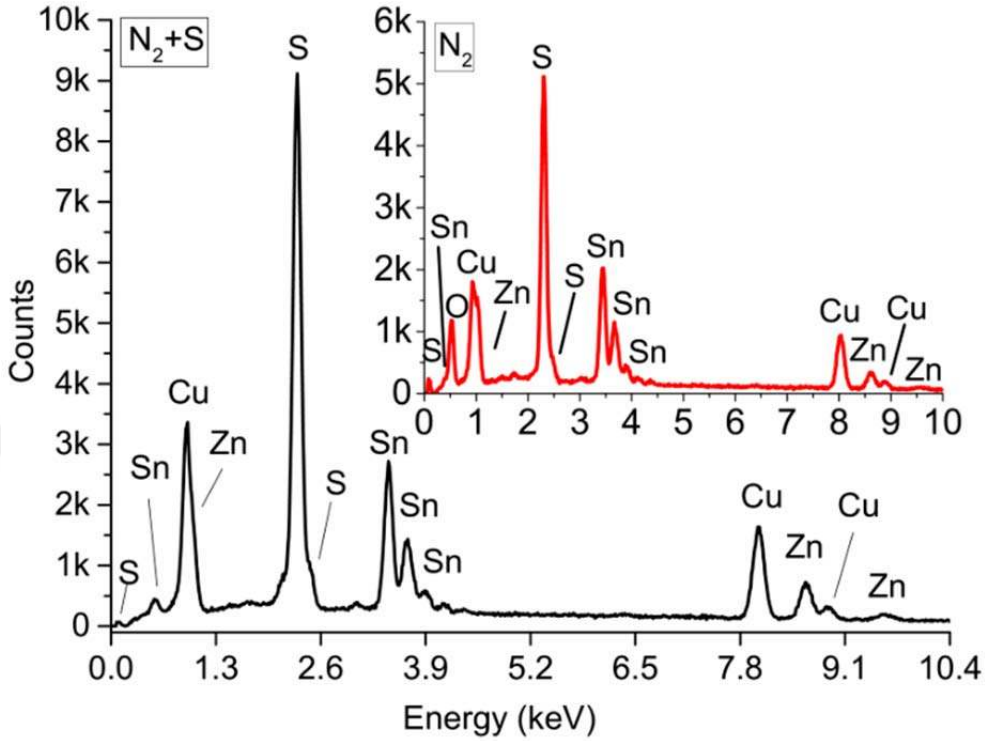

Figure 4.8. Field EDX plots of the films annealed in N_2 and N_2 + S vapor. By sulfurization treatment the elemental oxygen completely disappeared and the amount of S, Zn and Cu increased.

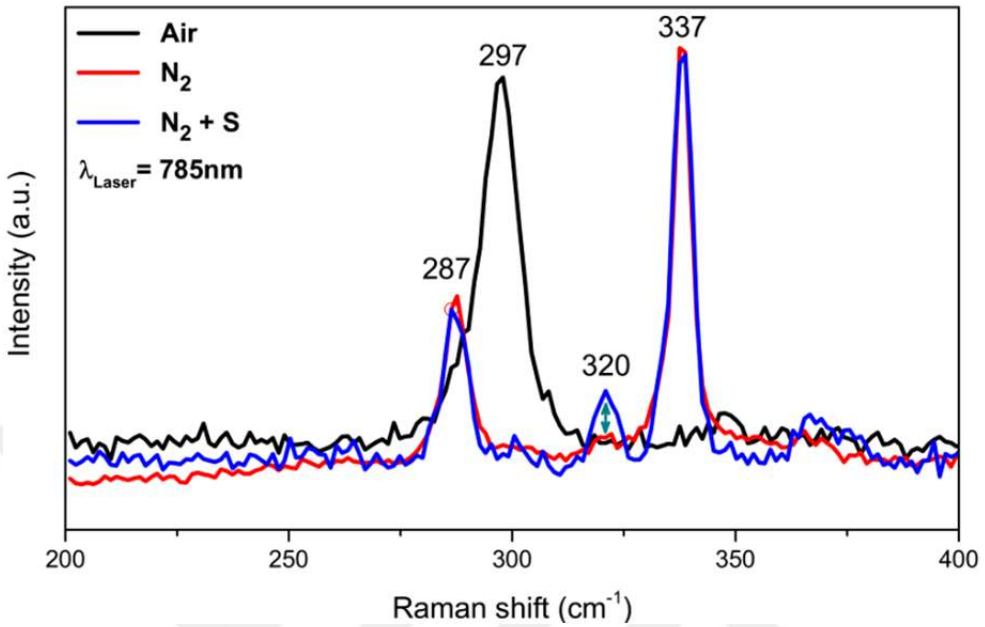

Figure 4.9. Raman spectra of the films annealed in air, N_2 and N_2 + S vapor. The undesired phase peak at 297.93 cm^{-1} disappeared by annealing in N_2 and CZTS peaks appeared.

4.1.7. Optical and electrical analysis

The resistance of the film annealed in the air was too high to achieve a reliable Hall Effect measurement using Ag paste electrode. However, the electrical measurements showed p-type conductivity for both films that annealed in N_2 and N_2 + S vapor. The sulfurization improved the electrical properties of CZTS thin film, the carrier concentration was 0.91E18 cm^{-3} and 1.22E18 cm^{-3} for N_2 and N_2 + S vapor annealing atmosphere, respectively. Even though the achieved crystallinity and the stoichiometry call for an increase in the carrier concentration, we have not observed a significant increase in the carrier concentration as a result of sulfurization. This suggests that, the open-circuit voltage and therefore the efficiency of a solar cell that uses a sulfurized absorber layer may not be high due to the relatively moderate carrier concentrations (Tajima et al., 2015) but it is still useable according to the literature (Mkawi et al., 2013; Xinkun et al., 2012).

Mobility and resistivity were 7.19 cm^2 V^{-1} s^{-1} and 0.71 Ω cm for the sulfurized film and 2.86 cm^2 V^{-1} s^{-1} and 2.39 Ω cm for the N_2 annealed film, respectively. Nevertheless, the mobility and resistivity of the sulfurized film compared to N_2 annealing is about three times higher and lower, respectively, and are consistent with the literature. That is, the grain size in the sulfurized film has increased and thus facilitated the carrier conduction and hopping to the nearest grains (Swami et al., 2013; Chaunhuri and Tiwari, 2012; Muhunthan et al., 2015). The band-gap of the films was determined by extrapolating the linear region of the $(\alpha h\upsilon)^2$ vs $h\upsilon$ and by taking the intercept on the $h\upsilon$ axis. As shown in Fig. 4.10, the optical band-gap energies for the films annealed in air, N_2 and N_2 + S vapor were 2.07, 1.58 and 1.51 eV, respectively. As one can see from the figure, the optical characteristics of the films annealed in N_2 and N_2 + S vapor are very close to each other as they are in XRD, Raman and EDX data. A significant optical improvement was achieved by annealing in N_2 compared to annealing in air (Park et al., 2013). However, the optical improvement provided by annealing in N_2 + S vapor is slightly higher than the improvement provided by annealing in N_2.

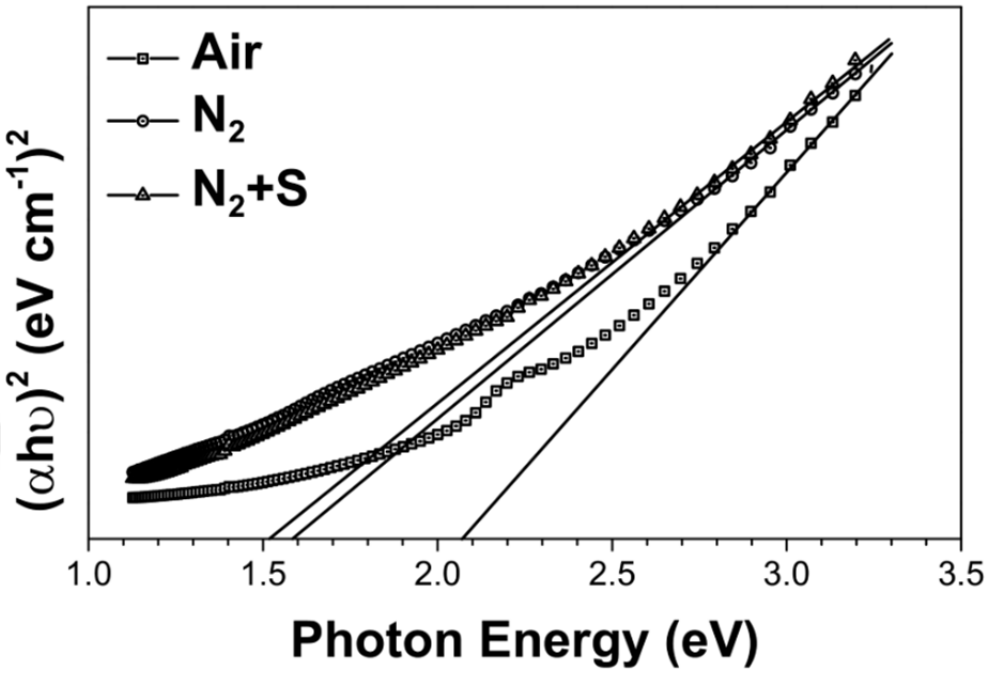

Figure 4.10. $(\alpha h\upsilon)^2$ - $h\upsilon$ plots of the films annealed in air, N_2 and N_2 + S vapor. A significant optical improvement was achieved by annealing in N_2. The optical improvement provided by annealing in N_2 + S vapor is slightly higher than the improvement provided by annealing in N_2.

4.2. Determination of crystallization threshold temperature

XRD plots of the samples annealed at 300, 400, 500, 525, 550 and 580 °C in Fig. 4.11 show that the main CZTS peak intensities increased with the temperature. There was not much improvement in the intensities for the samples annealed up to 400 ºC but the presence of three main peaks at 2θ = 28.36º, 47.20º and 56.04º, corresponding to the planes (112), (220) and (312) respectively, indicate the formation of kesterite CZTS phase structure. These intensities increased dramatically at 500 °C. There was no significant change in the intensities at higher annealing temperatures up to 580 °C. It appears that there is a threshold temperature value, lying between 400 and 500 °C, which cause significant increases in the intensities. There was no considerable change in the intensities at

annealing temperatures of 525, 550 and 580 °C. The highest peak intensities were obtained for the film annealed at 550 °C. The homogeneity of the films disappeared at temperatures higher than 580 ºC.

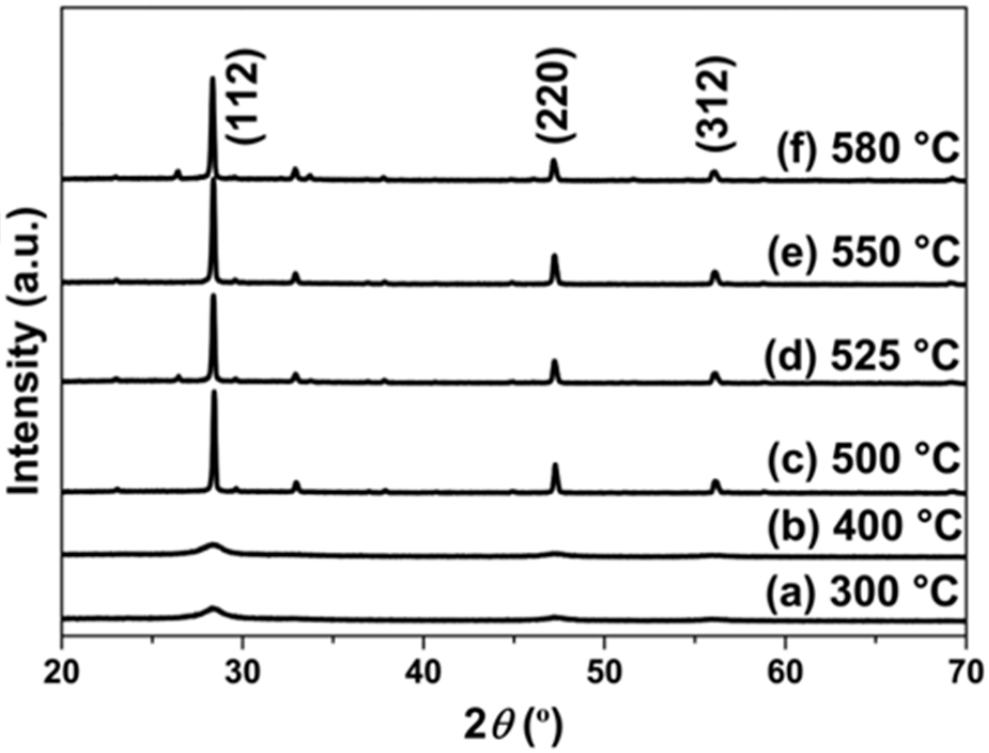

Figure 4.11. XRD plots of the samples annealed at (a) 300, (b) 400, (c) 500, (d) 525, (e) 550 and (f) 580 °C.

FE-SEM surface and cross-section images of the samples annealed at different temperatures in Fig. 4.12 show that the films annealed at 300 (a) and 400 ºC (b) have no granulation. Therefore, it is expected that their crystallizations are poor so that the intensity of the main peaks was very low as discussed above. There were also cracks in these two films showing that the quaternary structure was not completely formed. Starting from a temperature of 500 ºC (c), granulation was seen to have formed and therefore a significant increase in the crystallization had

begun. At higher annealing temperatures of 525, 550 and 580 ºC there was no significant change in particle size and overall surface morphology.

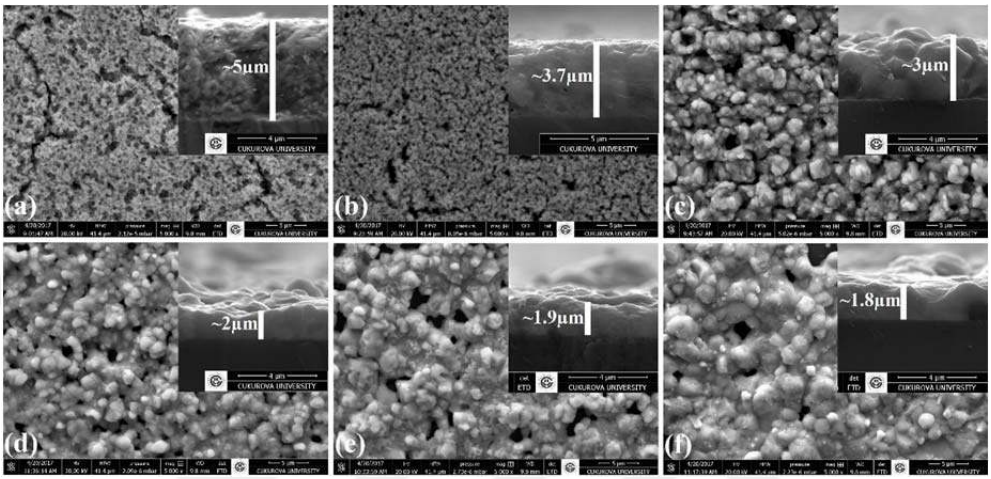

Figure 4.12. FE-SEM surface and cross-section images of the samples annealed at (a) 300, (b) 400, (c) 500, (d) 525, (e) 550 and (f) 580 °C.

Another important result was the variation in the film thickness which decreases depending on the annealing temperature. There was a huge decrease in the thickness of the films annealed at 400 and 500 ºC, respectively. There should be an important relation between the temperature and the reaction of the solution constituents. The decrease in thickness is probably due to the complete evaporation of the solvent residues and the loss of unbounded Sn and S. This phenomenon has been discussed in the EDX analysis below. For the films annealed at 525 (d), 550 (e) and 580 ºC (f) the thicknesses were almost the same. These results showed that the loss of material at 525 ºC was very limited and the resulting quaternary compound structure was stable. Thinner film which was sulfurized at 580 °C was slightly transparent and not useful as an absorber layer.

EDX analysis of the samples annealed at various temperatures is presented in Table 4.2. There is a huge amount of C, N and a small amount of O, Cl in the film structure annealed at 300 °C. As stated earlier, the presence of C and N can be

attributed to the incomplete evaporation of solvent and stabilizer. Even though boiling points of 2-metho and MEA are 125 °C and 170 °C, respectively, complete evaporation of these solvents at 300 °C may not be possible due to the thick and rigid structure of the film. Although not yet certainly ascertained, the presence of O in all films could be related to contact of the film surface and the surrounding air. The presence of Cl is probably due to the SLG substrate through the cracks on the film surface. For 400 °C, C and Cl contents completely disappeared and O and N ratios increased. The presence of N shows that 400 °C was not enough to evaporate all of N. As discussed above, the main XRD peaks of the films significantly increased and the granulation started when the annealing temperature was increased from 400 °C to 500 °C. Besides that, Sn and S ratios significantly increased. This phenomenon becomes even more meaningful as the CZTS structure becomes purer with the disappearance of undesired elements such as C, N and Cl. However, another undesired element, Si was appeared in the composition. The presence of Si is probably due to SLG as it is in the presence of Cl. Here it can readily be said that the increase in the annealing temperature gave rise to the evaporation of solvent residues and better formation of quaternary compound resulting in an increase in the amount of Sn and S in the composition. Therefore, by annealing the sample at 500 °C, the loss of Sn and S was largely avoided and better stoichiometry was achieved (Weber et al., 2009, 2010; Scragg et al., 2011). For 525 °C and higher temperatures, only O and Si undesired contents were observed. In the films annealed at 500, 525 and 550 °C, there was a significant increase in Cu and Zn ratios. Sn and S ratios are decreased and this can be attributed to material loss at a high annealing temperature of 580 °C. Elemental composition of stoichiometric and homogeneous film which annealed at 550 °C was obtained as Cu:Zn:Sn:S = 20.1:9.82:10.49:49.71.

Table 4.2. EDX analysis of the samples annealed at 300, 400, 500, 525, 550 and 580 °C.

	Atomic%					
	300 °C	400 °C	500 °C	525 °C	550 °C	580 °C
Cu	7.48	11.63	20.53	20.67	20.10	23.69
Sn	4.65	6.61	9.96	10.46	10.49	8.87
Zn	5.19	6.46	10.23	10.96	9.82	8.53
S	18.31	25.46	48.49	46.78	49.71	42.01
C	27.52	—	—	—	—	—
N	28.10	39.66	—	—	—	—
O	4.44	10.18	7.26	8.40	8.21	14.89
Cl	4.30	—	—	—	—	—
Si	—	—	3.53	2.73	1.67	2.01
	Ratio of composition					
Cu/(Zn+Sn)	0.76	0.88	1.01	0.96	0.99	1.36
Zn/Sn	1.11	0.97	1.02	1.04	0.94	0.96
S/metal	1.05	1.03	1.19	1.11	1.23	1.02

As can be seen from Table 4.3, samples annealed at 300 and 400 °C have an unstable electronic feature as they showed both p and n type semiconductor characteristics during measurements. For 500 °C and higher temperatures all samples were p-type and they have increasing carrier concentration with temperatures. Just as in other properties, the carrier concentration has also increased at temperatures higher than 400 °C. For the samples annealed at 500 and 525 °C, the carrier concentrations are almost equal but mobility and resistance increased by a factor of two and decreased by half, respectively. Better granulation due to increasing annealing temperature up to 525 °C resulted in better conductivity for carriers (Li et al., 2012; Muhunthan et al., 2015). It can also be seen that the sample annealed at 550 °C has better n, μ and ρ values. Although, the

carrier concentration of the film annealed at 580 °C is the high and the resistance is low, the low mobility may be due to the loss of Sn and S.

Table 4.3. n, μ and ρ values of the samples annealed at 300, 400, 500, 525, 550 and 580 °C.

T (°C)	n (cm^{-3})	μ ($cm^2\ V^{-1}\ s^{-1}$)	ρ (Ω cm)	Type
300	—	—	—	p-n
400	—	—	—	p-n
500	8.16E+17	2.48	3.08	p
525	9.12E+17	6.65	1.03	p
550	1.96E+18	5.58	0.57	p
580	6.75E+18	1.61	0.57	P

The discussions so far have shown an important detail: there must be a threshold temperature value which triggers the granulation between 400 and 500 °C. The XRD curves of the samples annealed at 400, 450, 465, 480 and 500 °C for the threshold temperature analysis in Fig. 4.13a show that there was no significant improvement in the crystallization for the samples annealed at 400 and 450 °C but crystallization started to increase at 465 °C. The samples annealed at 465 and 480 °C have two and four times higher peak intensities than the sample annealed at 450 °C, respectively. When the temperature was increased to 500 °C, the peak intensities increased about five times.

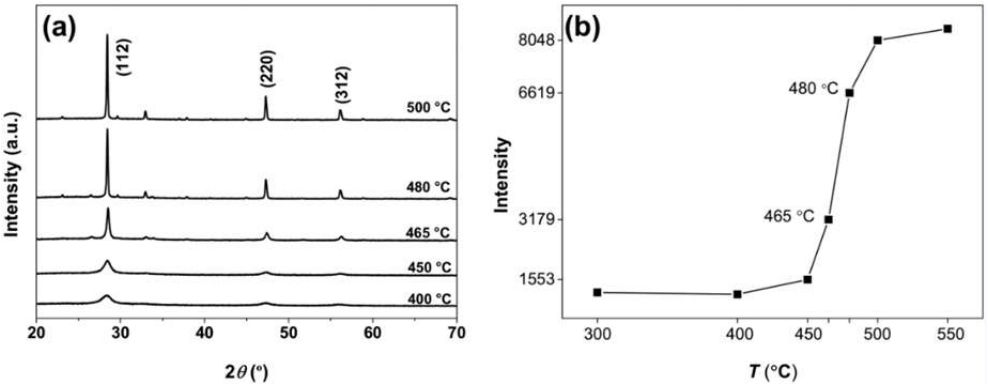

Figure 4.13. (a) XRD plots of the samples annealed at 400, 450, 465, 480 and 500 °C and (b) annealing temperature (*T*) and (112) plane peak intensity plot.

Fig. 4.13b shows the relation between annealing temperature (*T*) and peak intensity of (112) plane. A small increase of 15 °C in the temperature greatly increased the intensity. As can be seen in Fig. 4.14b, agglomeration prompting the increase in crystallinity was formed. These two results show that the crystallization has improved after annealing at a temperature of 465 °C. When the temperature is further increased by an additional 15 degrees to 480 °C, the peak intensity is doubled and grain formation is much more pronounced, as shown in Fig. 4.14c. By increasing the temperature to as much as 500 °C, the peak intensity of (112) plane can be shown to have increased to the level at which it is almost stable. XRD and FE-SEM analysis clearly show that crystallinity improvement starts at the annealing temperature of 465 °C.

AFM images of the samples annealed at (d) 450, (e) 465 and (f) 480 °C are presented in Fig. 4.14. Grain density increased with temperature. The cracks on the sample annealed at 450 °C can also be seen in AFM image. The cracks disappeared and turned into pin holes as the temperature increased by 15 °C. There must have been an increase in the crystallite size which promotes crystallization and leads to granulation. At a temperature of 480 °C, the size of the pin holes in the film surface decreased and the grain density increased. Increase in the crystallization

and granulation due to temperature is seen as an increase in surface roughness. Typical granular structure was first observed for the sample annealed at 480 °C and the grain size measured to be 1.5-2.5 µm as indicated in Fig. 4.14c and f.

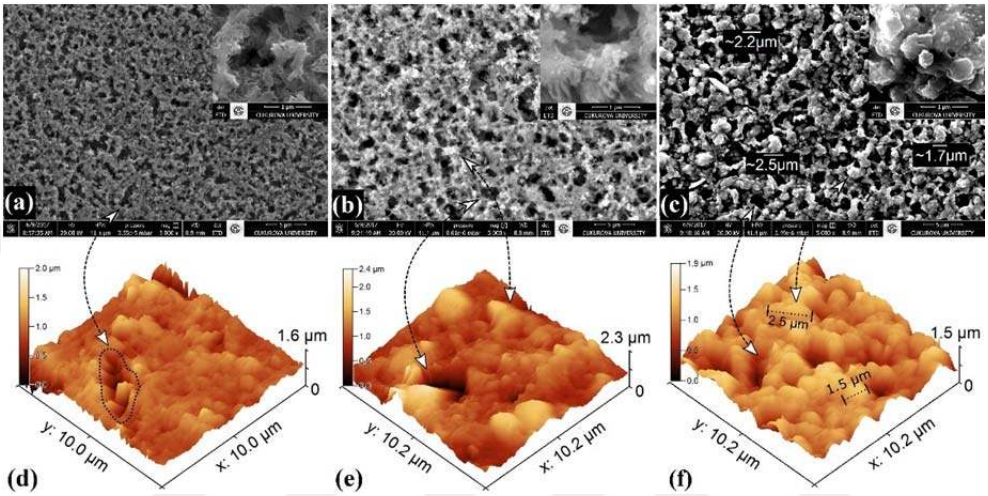

Figure 4.14. FE-SEM surface and AFM images of the samples annealed at (a, d) 450, (b, e) 465 and (c, f) 480 °C.

The average crystallite size of the film calculated using Scherrer's formula;

$$D = \frac{0.9\lambda}{\beta \cos\theta} \tag{4.1}$$

where λ is the X Rays wavelength (Cu Kα = 1.5418 Å), θ is Bragg diffraction angle and β is the full width at half maximum (FWHM) of the diffraction peak at 2θ. β and θ were obtained from XRD raw data using OriginPro data analysis and graphing software. D_{AV} is the average of the D values of (112), (220) and (312) planes and FWHM versus the annealing temperature for (112) plane are plotted in Fig. 4.15. D_{AV} significantly increased and FWHM decreased while the temperature increased from 450 to 465 °C, which explains the reason of higher main peak intensities. An increase in temperature of 15 °C boosted the

crystallite size and main peak intensities. Another significant increase in D_{AV} was observed at a temperature of 480 °C while there were no critical changes at higher temperatures.

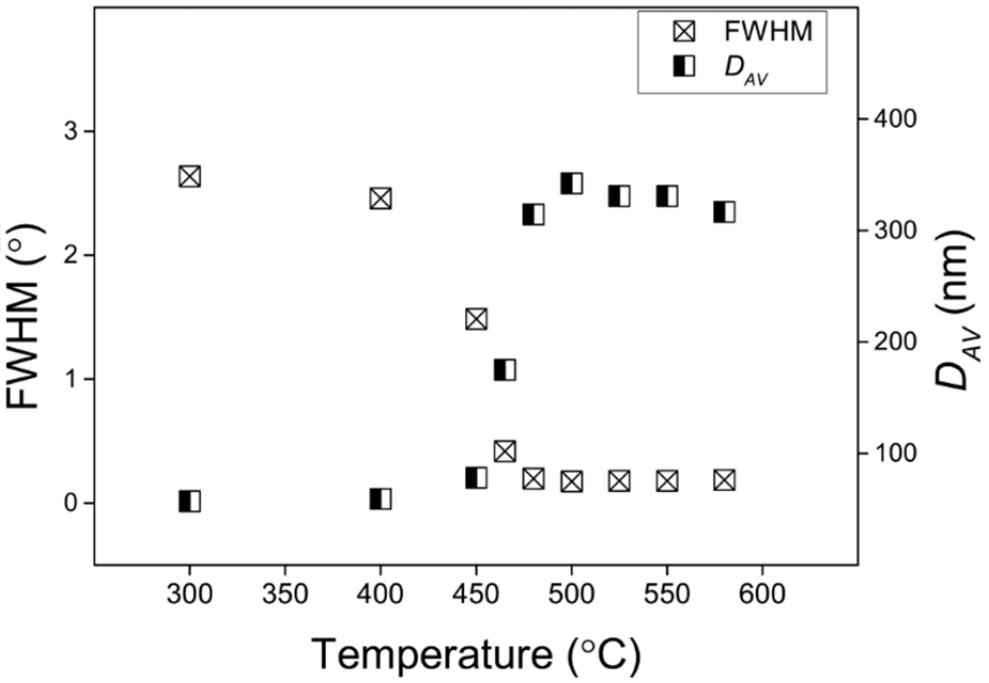

Figure 4.15. The variation of D_{AV} and FWHM with annealing temperatures.

In Table 4.4, (112) plane peak position (2θ), related crystallite size (D), microstrain (ε) and dislocation density (δ) depending on annealing temperatures are listed. Microstrain (ε) was calculated from the following equation;

$$\varepsilon = \frac{\beta \cos\theta}{4} \tag{4.2}$$

and dislocation density (δ) calculated using Williamson and Smallman relation;

$$\delta = \frac{n}{D^2} \tag{4.3}$$

where n is equals to unity. While dislocation density (δ) is very high for the films annealed at 300 °C and 400 °C, their electronic features were unstable as discussed above. However, a sudden decrease in the dislocation density (δ) at 500 °C significantly improved the electronic features. The film begins to show stable p-type semiconductor properties. Crystallite size (D) and carrier concentration (n) increased while residual microstrain (ε) and resistivity (ρ) decreased with temperature. This tremendous increase in crystallite size (D) also reveals the great increases in crystallinity as discussed above. There are no significant variations at the main XRD peak intensities and crystallite sizes of CZTS thin film after certain annealing temperatures.

Table 4.4. (112) plane peak position (2θ), related crystallite size (D), microstrain (ε) and dislocation density (δ).

T (°C)	2θ (°)	D (nm)	ε (E-3)	δ
300	28.30	58.95	11.15	1.17E-03
400	28.29	63.21	10.40	1.02E-03
450	28.40	51.84	6.29	3.72E-04
465	28.52	184.08	1.78	2.95E-05
480	28.44	388.82	0.84	6.61E-06
500	28.42	441.71	0.74	5.13E-06
525	28.38	431.17	0.76	5.38E-06
550	28.38	431.17	0.76	5.38E-06
580	28.34	411.57	0.79	5.90E-06

Raman scattering spectra for the samples annealed at 450, 465 and 480 °C were shown in Fig. 4.16. All the samples in Fig. 4.16a excited using 738 nm laser exhibit one dominant Raman peak at 331.4 cm^{-1} which shows the presence of local

disorders caused by possible Cu-poor and Zn-rich regions in our samples (Fontane et al., 2012; Valakh et al., 2013). When the temperature is increased by 15 °C to 465 °C, a large increase in peak intensity at this point was observed. The inset image of Fig. 4.16a shows that there were also weaker contributions around 287 cm^{-1}, indicating that peaks tend to be sharper with temperature. There were secondary phase peaks for the sample annealed at 450 °C. These intense peaks at 455, 656, 703 and 778 cm^{-1} were formed by $Cu_{2-x}S$ phase and unreacted thiourea (Chavda et al., 2016). It is clear that the annealing temperature had a significant effect on the stoichiometry. A 15 °C increase in the annealing temperature eliminated any undesired phase and caused another CZTS peak to appear at 287 cm^{-1}. A further increase in the temperature to 550 °C fixed the peak positions at 287 and 337 cm^{-1}, the characteristic CZTS peak positions. All of the samples excited using 532 nm laser to distinguish CZTS, Cu_xS and Cu_2SnS_3 phases in Fig. 4.16b exhibited dominant Raman peaks at about 287 and 338 cm^{-1}. Main CZTS peaks of the samples annealed at 450 °C and 465 °C was obtained at 335 and 336 cm^{-1} which shows temperature dependent shift to 338 cm^{-1}. These two samples also have an undesired phase of $Cu_{2-x}S$ at 470 and 472 cm^{-1}, respectively. When the temperature is increased to 480 °C, undesired $Cu_{2-x}S$ pahse disappeared.

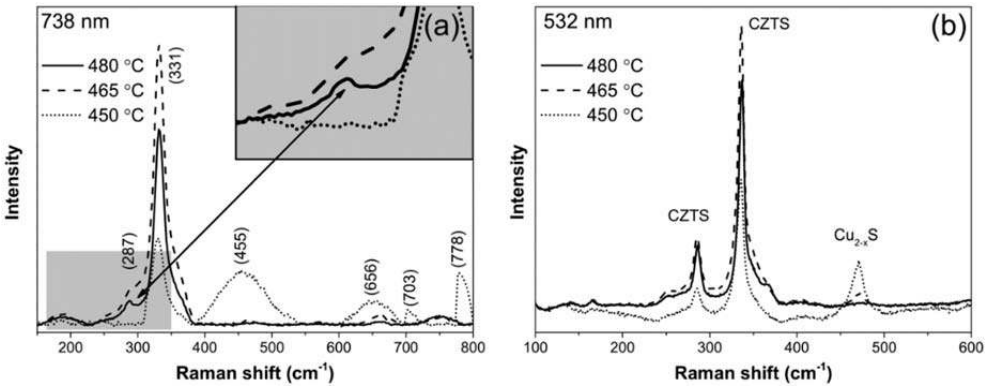

Figure 4.16. Raman measurements of the samples annealed at 450, 465 and 480 °C using (a) 738 nm (b) 532 nm laser.

The optical absorption coefficient α was calculated using the following formula;

$$\alpha = \frac{1}{d} \ln \frac{(1-R)^2}{T} \tag{4.4}$$

where d is the film thickness, R is the reflectance and T is the transmittance of the films. Optical band-gap energies of the films annealed at 450, 465 and 480 °C were determined by extrapolating the linear region of the $(\alpha h\upsilon)^2$ vs $h\upsilon$ and by taking the intercept on the $h\upsilon$ axis. Fig. 4.17 shows transmittance and *Eg* increased with the annealing temperature. Band gaps were 1.38, 1.46 and 1.48 eV for films annealed at 450, 465 and 480 °C, respectively. With a temperature increase of 15 °C, the transmittance and the *Eg* increased by 2% and 0.8 eV, respectively. The main increase in transmittance was achieved by the formation of granulation with an increase in temperature to 480 °C, and thus an increase in crystallization.

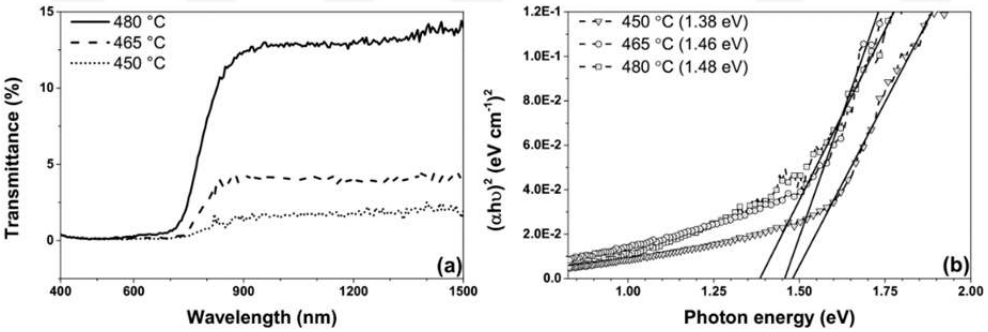

Figure 4.17. Transmittance plots and (b) optical band-gap energies of the films annealed at 450, 465 and 480 °C.

So far, as can be seen from Fig. 4.18, it has been found that the lowest drying temperature is 300 °C, while the lowest and the highest annealing temperatures are 465 °C and 550 °C, respectively, for CZTS thin films we produced by the spin coating method.

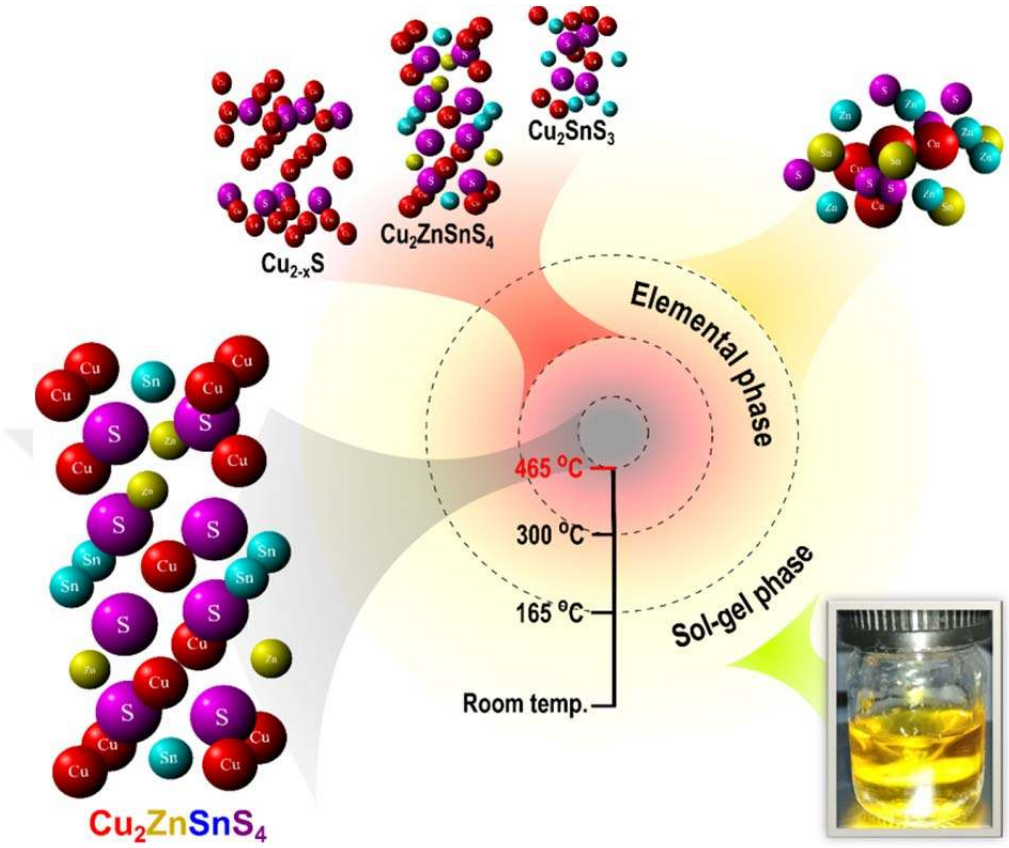

Figure 4.18. Schematic representation of the drying and annealing heat parameters of CZTS films we produced by spin coating method.

For the time-dependent structural analysis, we doubled the predetermined annealing time and compared the results. XRD plots of the samples annealed at 550 °C for (a) 30 and (b) 60 min are shown in Fig. 4.19. Annealing time did not cause a significant change except a slight decrease in the main CZTS peaks. This minor decrease in the peaks can be attributed to a small amount of Sn and S loss due to longer annealing at high temperature as can be seen in Table 4.5. Stoichiometry of the film is disturbed and has adversely affected the crystallinity. In Fig. 4.20, FE-SEM surface images of the films annealed at 550 °C for (a) 30 and (b) 60 minutes show that grain size and thickness of the films are almost the same.

The FWHM values of the main (112) plane peaks of the samples were calculated as 0.180° and 0.182°, respectively. For longer annealing times of more than 60 minutes, stoichiometry and homogeneity of the films are significantly disturbed.

Table 4.5. EDX analysis of the films annealed at 550 °C for 30 and 60 min.

	Atomic%						Rate of composition		
	Cu	Sn	Zn	S	O	Si	Cu/(Zn+Sn)	Zn/Sn	S/metal
30 min	20.10	10.49	9.82	49.71	8.21	1.67	0.99	0.94	1.23
60 min	20.01	9.83	10.71	46.80	9.36	3.30	0.97	1.09	1.15

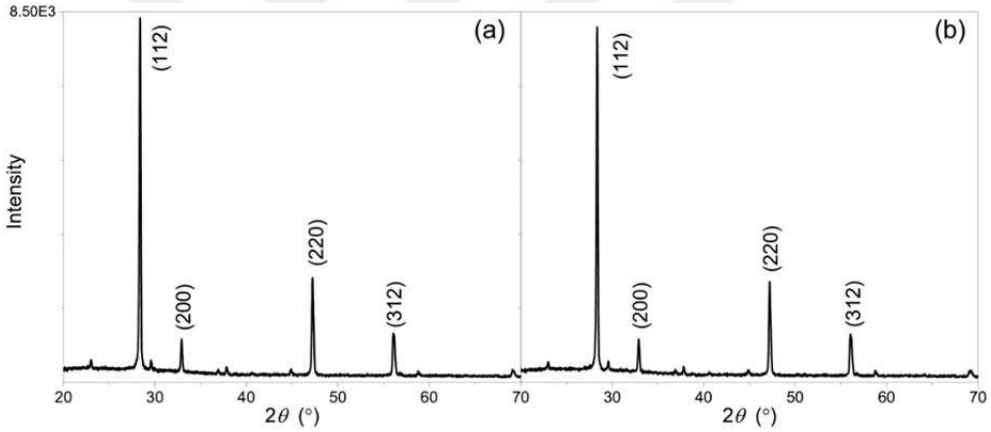

Figure 4.19. XRD patterns of the films annealed for (a) 30 and (b) 60 min.

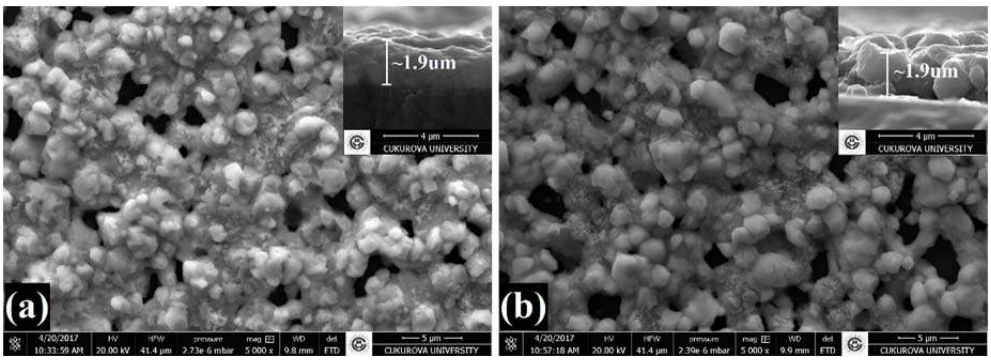

Figure 4.20. FE-SEM surface and cross-section images of the films annealed at 550 °C for 30 and 60 min.

4.3. Nonlinear optical characterization results

In MOLTECH-Anjou laboratory we were capable to achieve the third-order nonlinear optical susceptibilities $\chi^{(3)}$ of CZTS thin films deposited by spin-coating technique via the THG method by means of the rotational Maker fringes technique which has been developed with the aim of measuring the nonlinear coefficients of the medium. The Maker fringes are formed by an alternating sequence of maxima and minima of the transmitted intensity as a function of the incident angle (This process is featured in Fig. 4.21, with θ_i is the incident angle, n_0 the refractive index of the material and d is the thickness) (Maker et al., 1962). The detail of the THG setup was well described in our previous published paper (Chtouki et al., 2019).

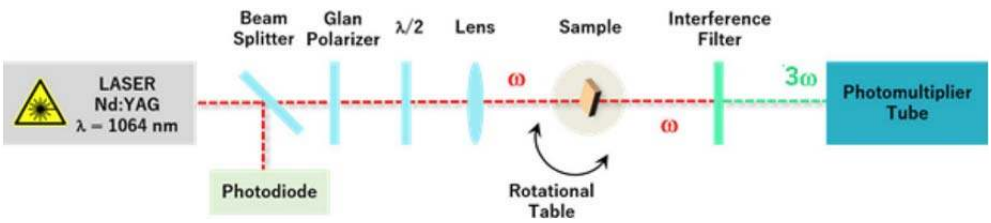

Figure 4.21. The Maker fringes technique principle representation for the case of THG.

In order to determine the third-order nonlinear susceptibility $\chi^{(3)}$, the model of Kubodera and Kobayashi, taking into account the high absorption of our films was chosen (Kubodera and Kobayashi, 1990). We have compared the THG signal of the studied sample and that of the silica, which was a reference material (we used a fused silica plate with a thickness of 1 mm). The used relationship to determine the magnitude value of the third order nonlinear susceptibility is written in the following form:

$$x^{(3)} = x^{(3)}_{silica}\left(\frac{2}{\pi}\right)\left(\frac{l^{coh}_{silica}}{d}\right)\left(\frac{(\alpha d/2)}{1-e^{-\frac{\alpha d}{2}}}\right)\left(\frac{I^{3\omega}}{I^{3\omega}_{silica}}\right)^{1/2}$$

Where: $x^{(3)}_{silica}$ is the NLO susceptibility for the fused silica glass which is equal to 2.0E-22 m^2 V^{-2} , (d) is the thickness of the film, (α) is the absorbance coefficient, l^{coh}_{silica} is the coherent length for silica ($l^{coh}_{silica} = \frac{\lambda}{6|\, n_{s\omega - n_\omega}|} = 6.7\ \mu m$) while $I^{3\omega}_{silica}$ and $I^{3\omega}$ represent the THG intensities of silica and sample respectively (Gubler and Bosshard, 2000; Kajzar et al., 2001).

The experimental variation of THG intensity in the function of the angle of the incident beam on CZTS thin films for different temperatures are represented in Fig. 4.22. An oscillatory signal with many fringes is displayed by the curves. The THG intensities of the elaborated films were found to be higher than the response of the substrate, indicating thus the efficiency of the signal generated by the third harmonic generation method. We evaluated the third-order nonlinear optical susceptibility values of CZTS thin films, by comparing the THG signal of silica and that one of our elaborated samples. The values of the third-order nonlinear optical susceptibility are all included in Table 4.6.

Table 4.6. Results of NLO Susceptibility $\chi^{(3)}$ obtained for different annealing temperatures for CZTS thin films prepared by spin-coating technique.

Sample	Thickness (nm)	Polarization	Annealing Temperature (°C)	$\chi^{(3)}$ (m^2 V^{-2})
CZTS	350	S	300	1.37E-20
	410		400	1.25E-20
	370		500	1.84E-20
	310		550	1.10E-20

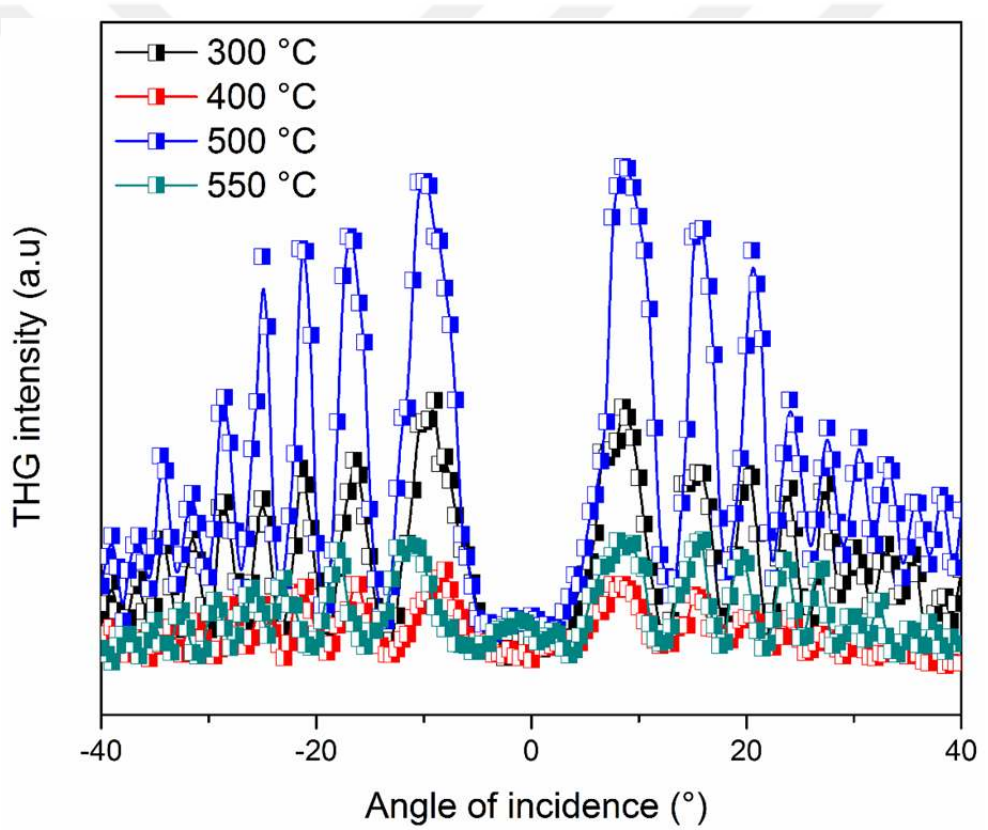

Figure 4.22. THG intensity of CZTS thin films elaborated by spin-coating and annealed at different temperatures (300, 400, 500 and 550°C) as a function of incident angle for the S-polarization laser beam.

We remarked that the highest value of the third order nonlinear optical susceptibility is recorded for CZTS thin film deposited at the annealing temperature of 500 °C (1.84E-20 $m^2 V^{-2}$), against the lowest value is observed for the film at 550 °C (1.10E-20 $m^2 V^{-2}$). Whereas the $\chi^{(3)}$ values for the CZTS thin films deposited at 300 and 400 °C have been estimated to be 1.37E-20 and 1.25 E-20 $m^2 V^{-2}$. We can achieve that the differences in the values for the third-order nonlinear optical susceptibility of CZTS thin films can be related to the changes in the structural, morphological and optical characteristics due to the impact of annealing temperature which can influence the properties of CZTS films as demonstrated above.

4.4. Analytical modelling results

4.4.1. SEM analysis of the CZTS/CdS/ZnO device

SEM images in Fig. 4.23(a) and (b) show the surface morphologies of uncoated and ZnO coated CZTS (S2) thin films. Approximately 300 nm thick (Kuo and Hsieh, 2014) ZnO layer adsorbed on to CZTS grains was increased the surface roughness. Each sample of S1-S7 in Table 4.7 was fabricated on 2.5x2.5 cm Mo/glass substrates then divided into individual cell islands by mechanical scribing, and the structures accomplished with common back and separated top Ag metal contacts (Fig. 4.23(d)). Crystallinity diffractograms of CdS and ZnO thin films could not be obtained because the thicknesses of the films were below 100 nm.

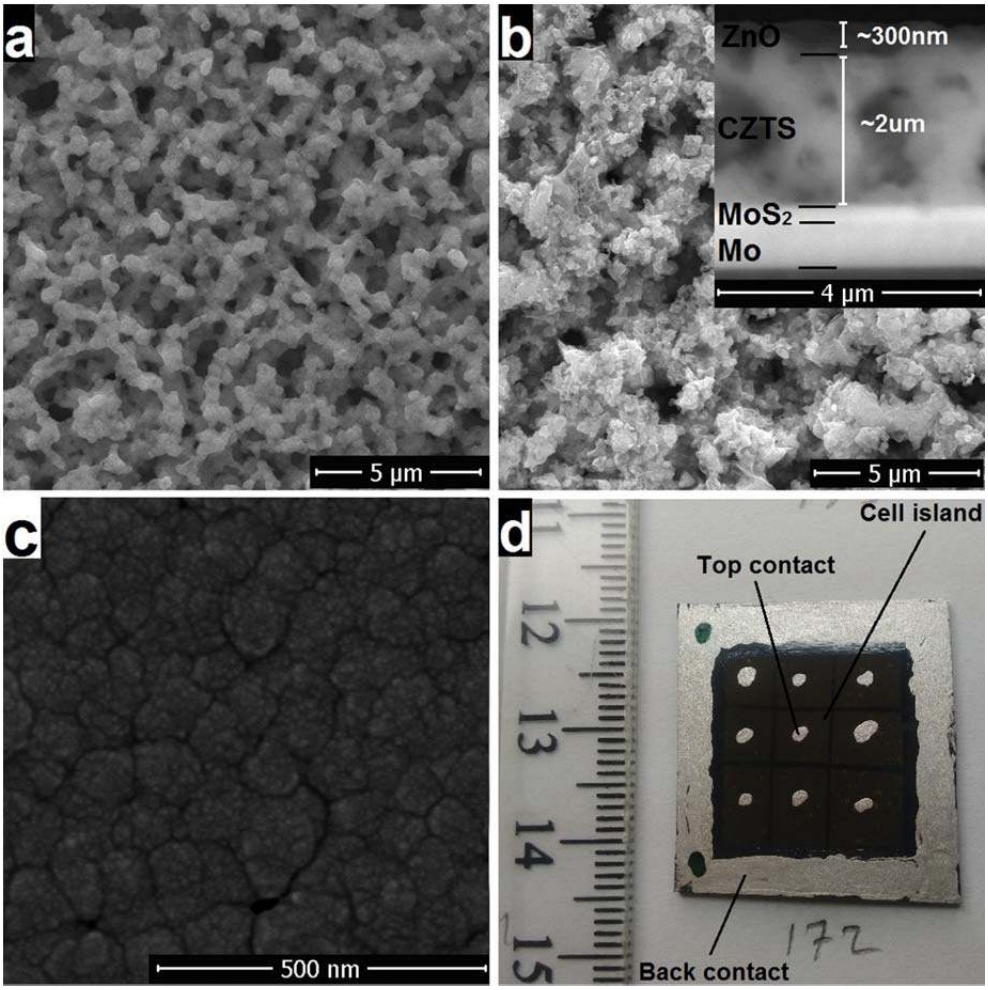

Figure 4.23. SEM images of (a) CZTS, (b) ZnO coated CZTS and (c) CdS thin film surfaces. (d) CZTS/CdS/ZnO device fabricated on 2.5x2.5 cm Glass/Mo substrate.

4.4.2. I-V analysis of the CZTS/CdS/ZnO device

Dark I-V output characteristics of the samples S1-S7 in Fig. 4.24(a) revealed that the S1 has poor rectifying behavior and therefore poor junction properties compared to S2. This improvement is related to KCN treatment which removing of undesired phases on the CZTS surface of S2. The increment of ZnO thickness in S3 has increased the resistance which caused the diode to act as a

resistance under the limited applied voltage. The forward diode current was increased by changing the solvent from isopropyl alcohol to 2-metho in the ZnO preparation process of S4. This phenomenon is related to the increase in solubility of Zn ac. salt in 2-metho (Foo et al., 2014). ZnO crystallinity and hence heterojunction was improved by replacing the solvent and limiting the thickness. So far, all ZnO layers on CZTS are annealed at 450 °C. The forward diode current of S5 in Fig. 4.24(b) is reduced compared to S4 because of its weak crystallinity of the ZnO layer which annealed at 200 °C. The addition of the CdS buffer interlayer (Fig. 4.24(c)) in S6 contributed a slight improvement in forwarding current (Monserrat et al., 2018). Reducing the ZnO thickness in S7 is significantly increased the forward diode current as seen in Fig. 4.24(c). Based on the I-V output characterization results, it can be concluded that the most important fabrication parameters that improve the rectifier characteristics of heterojunctions are the crystal structure and thickness of the ZnO layer. However, the conclusion we reached as a result of the measurements made so far, gives a limited idea of diode properties and therefore the heterostructure. A further analysis was made to determine the diode properties in the following section of the study.

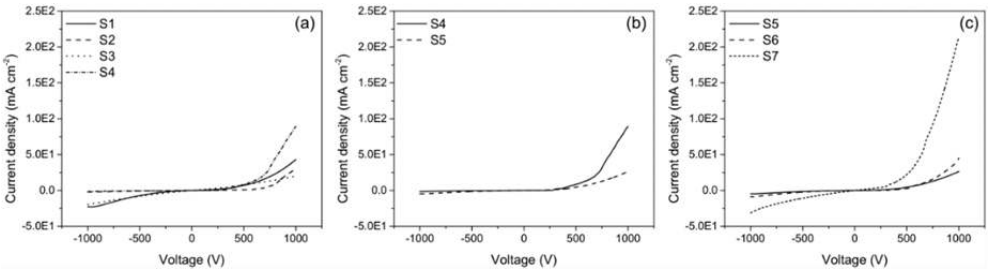

Figure 4.24. Dark I-V output characteristics of the S1-S7 heterojuctions.

Fig. 4.25 shows the I-V measurement process of the heterojunction under 100 mW/cm^2 solar illumination (AM1.5G).

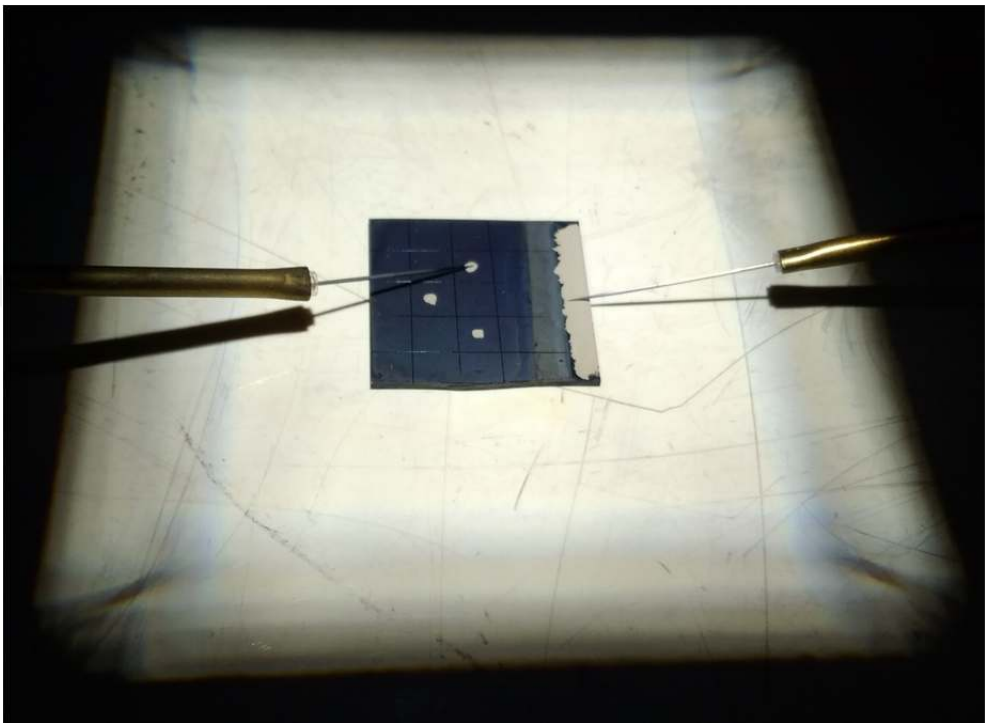

Figure 4.25. I-V measurement process of the heterojunction under 100 mW/cm^2 solar illumination (AM1.5G).

In Fig. 4.26, it was seen that the solar cell efficiency of the CZTS/CdS/ZnO heterojunction (S7). The very low photocurrent and FF obtained from the solar cell is a negative result of impurities at the interface and in the CZTS. It was observed that the efficiency decreased to half after the cell was re-measured after waiting 60 days. The voltage value remained almost the same, but the photocurrent decreased by half.

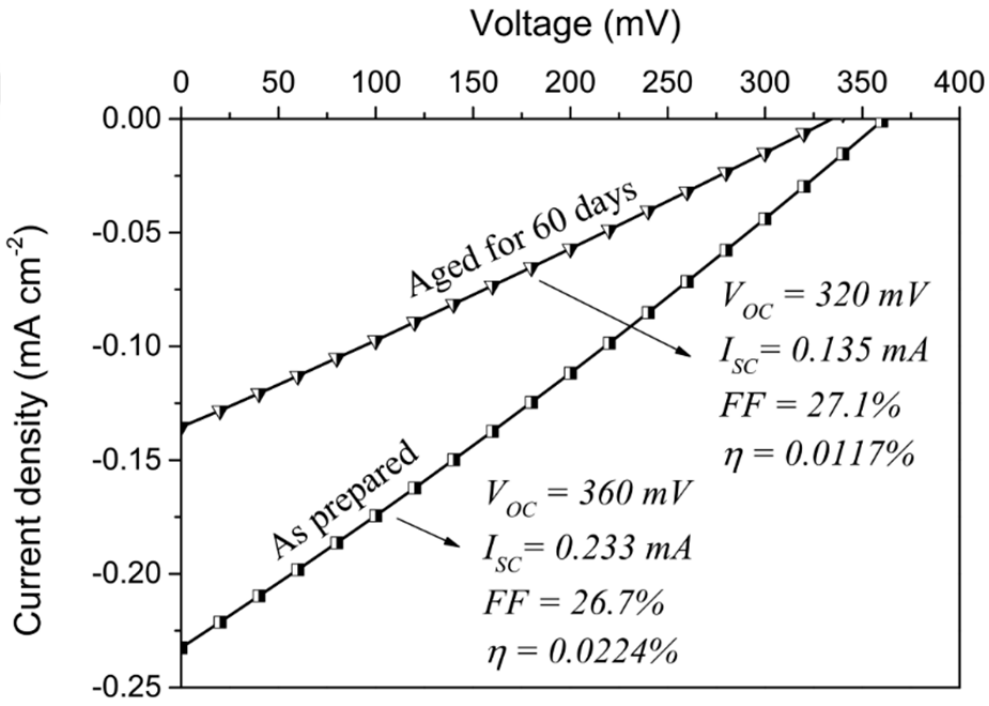

Figure 4.26. Light I-V output characteristics of the CZTS/CdS/ZnO (S7) heterojuction.

In the following sections, the diode current equation of CZTS/CdS/ZnO (S7) will be modelled using only the experimental I-V output data and electrostatic parameters.

4.4.3. Two points method

In this method, it was assumed that only diffusion process is responsible for total current in CZTS/CdS/ZnO heterojunction diode and $I_d = I_{DIFF}$ diode current can be represented with simple "one exponential" as in Eq. (1)

$$I_d = I_0\left(\mathrm{e}^{\mathrm{q}V_d/n\mathrm{k}T} - 1\right) \quad (1)$$

where I_{DIFF} is diffusion current, I_0 is diode saturation current, n is diode ideality factor, k is Boltzmann constant, T is temperature and q is electron charge. Here one can approximately calculate I_0 by substituting V_d and I_d taken from positive dark I-V data and an estimated value of n into the equation. Alternatively, n and therefore I_0 can be found more precisely by the trial-and-error method using carefully selected two (V_d, I_d) points from the curve and choosing n by; (*i*) finding two different (V_{dk}, I_{dk}) and $(V_{d(k+1)}, I_{d(k+1)})$ $(1 \leq k \leq 5)$ data points with help of three main tangent lines roughly pattern the dark I-V curve as shown in Fig. 4.27(a), (*ii*) putting them into expressions below

$$I_{d(k+1)}/\mathrm{e}^{(\mathrm{q}V_{dk}/n\mathrm{k}T)} - 1$$

And

$$I_{dk}/\mathrm{e}^{(qV_{d(k+1)}/nk\mathrm{T})} - 1$$

where $\frac{\mathrm{k}T}{\mathrm{q}} = 0.0259\,V$ $(T = 300\,K)$ is thermal voltage, (*iii*) plotting both results versus selected n values in the range of 1 to 10 (0.01 step) to find the intersection point of curves which gives actual n. Substituting the n into the following equation

$$I_0 = \frac{I_{dk}}{e^{V_{dk}/0.0259n} - 1} \quad (2)$$

or

$$I_0 = \frac{I_{d(k+1)}}{e^{V_{d(k+1)}/0.0259n} - 1} \quad (3)$$

gives I_0. The lowest n from the intersection point of the curves drawn using (V_{d2}, I_{d2}) and (V_{d3}, I_{d3}) points in Fig. 4.27(b) and related I_0 were evaluated as 6.12 and 9.430E-4 A, respectively.

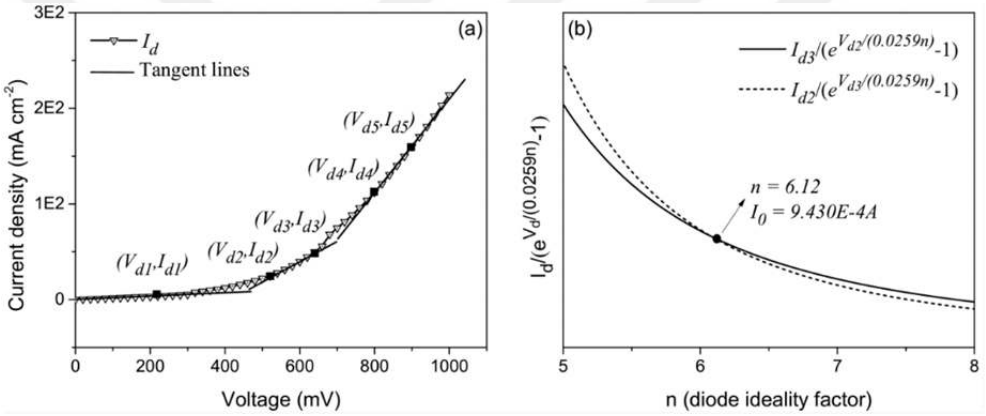

Figure 4.27. (a) Dark I-V and (V_d, I_d) points of CZTS/CdS/ZnO diode with tangent lines and (b) extraction of the n and I_0. The lowest n from the intersection point of the curves drawn using (V_{d2}, I_{d2}) and (V_{d3}, I_{d3}) points.

This method gives an approximate value for the I_0 and n variables of the diode. The current (I_1) plotted with these variables was not matched I_e experimental result. Modifying the current by simply altering n or I_0, two different but closer I_2 and I_3 current plots were achieved and compared with I_1 and I_e in Fig. 4.28(a) and (b), respectively. Another current (I_4) plotted by changing both n and I_0, was also attained and compared in Fig. 4.28(c). Both I_2 and I_4 display closer characteristics to I_e, while I_3 was slightly different.

In this method, the closest I_2 current which renamed as I_{m1} was plotted with $n = 7.12$ and $I_0 = 9.430E - 4\ A$, and is still not matching well with I_e, specifically in negative voltage region (Fig. 4.28(d)). Here one can easily conclude that the ideal diode equation (Eq. (1)) is not sufficient to model real diode I-V output characteristics.

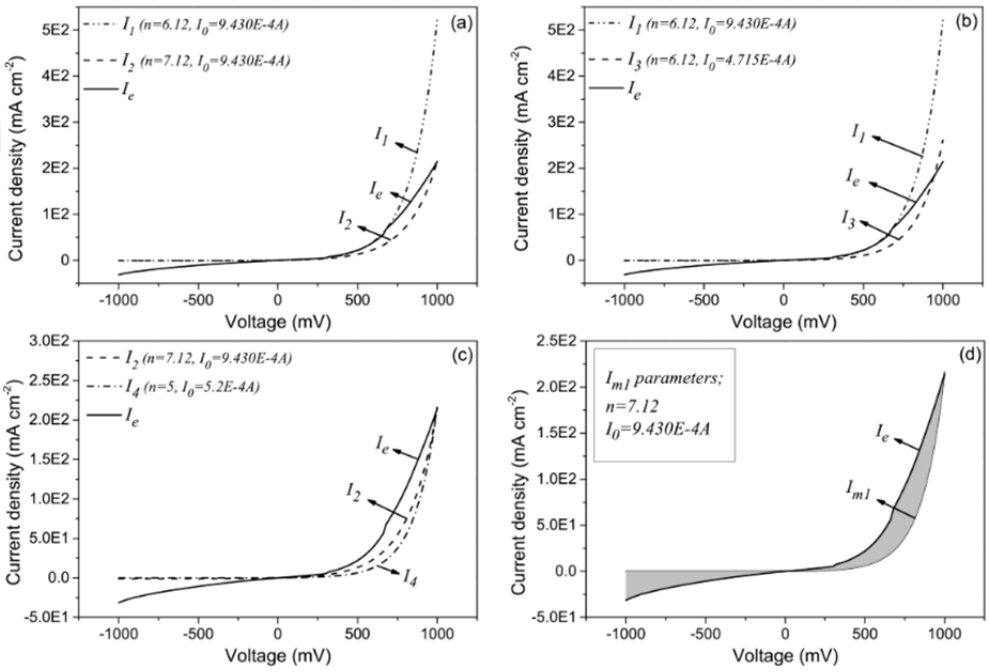

Figure 4.28. I_e and I_1 currents were compared with modified current (a) I_2 and (b) I_3 by simply altering n or I_0, respectively. (c) The effects of change in both n and I_0 were investigated by plotting and comparing I_4 with I_2 and I_e. Both I_2 and I_4 display closer characteristics to I_e, while I_3 was slightly different. (d) "Filled area curve" comparison of I_e and I_{m1} (I_2) show unmatching regions in detail.

4.4.4. Two exponentials method

In "*Two points method*" above, only I_{DIFF} diffusion current, which is dominant when V_d greater than a few kT/q , was considered as the main current source of the device. A more accurate diode model should also include I_{R-G}

thermal recombination-generation current which is dominant in weak voltage region of the curve as represented in Eq. (4).

$$I_d = I_{DIFF} + I_{R-G} \quad (4)$$

Hence, the new current model, which is created with two I_{01} and I_{02} saturation currents and related n_1 and n_2 diode ideality factors, will consist of two separate exponentials expressions as in Eq. (5).

$$I_d = I_{01}\left(e^{q(V_d)/n_1 kT} - 1\right) + I_{02}\left(e^{q(V_d)/n_2 kT} - 1\right) \quad (5)$$

Here I_{01} and I_{02} can be determined using tangent lines of n_1 and n_2 regions in the $Log(I_d) - V_d$ curve (Fig. 4.29(a)) for $V_d = 0$

$$\ln(I_{DIFF}) = \ln(I_{01}) + \frac{qV_d}{n_1 kT} \quad (6)$$

$$\ln(I_{R-G}) = \ln(I_{02}) + \frac{qV_d}{n_2 kT} \quad (7)$$

and n_1 and n_2 can be calculated via Eq. (8) and (9)

$$n_1 = \frac{V_{d2} - V_{d1}}{(kT/q)\ln(I_{d2}/I_{d1})} \quad (8)$$

$$n_2 = \frac{V_{d4} - V_{d3}}{(kT/q)\ln(I_{d4}/I_{d3})} \quad (9)$$

where $(V_{d1,2}, I_{d1,2})$ and $(V_{d3,4}, I_{d3,4})$ points were taken from linear parts of Log(I)-V curve in n_1 and n_2 region, respectively. n_1 and n_2 were calculated as 5.72 and 5.98, and I_{01} and I_{02} were measured as 9.67E-4 A and 1.13E-3 A, respectively.

The current I_1 plotted in Fig. 4.29(b) using n_1, n_2, I_{01} and I_{02} display slightly better characteristics than I_e.

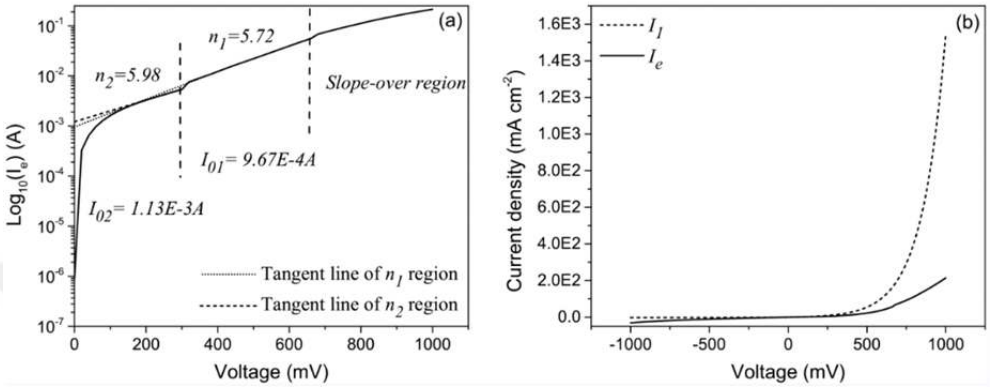

Figure 4.29. The diode current I_1 was calculated using I_{01} and I_{02} (a) extracted from $Log(I_d) - V_d$ curve using tangent lines of n_1 and n_2 regions. (b) The current I_1 plotted using n_1, n_2, I_{01} and I_{02} display slightly better characteristics than I_e.

By altering only n_1 and n_2 (Fig. 4.30(a)) or I_{01} and I_{02} (Fig. 4.30(b)), closer I_2 and I_3 current curves can be attained, respectively. I_4 plotted by changing all n_1 n_2, I_{01} and I_{02} in Fig. 4.30(c) also exhibits closer, but still not sufficiently close characteristic to I_e. The closest current curve to I_e was I_2 with $n_1 = 8.22$ and $n_2 = 8.45$. "Filled area curve" comparison of I_2 (I_{m2}) and I_e in Fig. 4.30(d) display that mismatching regions are almost the same as in the "*Two points method"*. Although the two exponentials current equation (Eq. (5)) provides a better matching result, it is still not sufficient to model the real diode characteristic. There are still important characteristic differences between the two plots specifically in negative voltage regions.

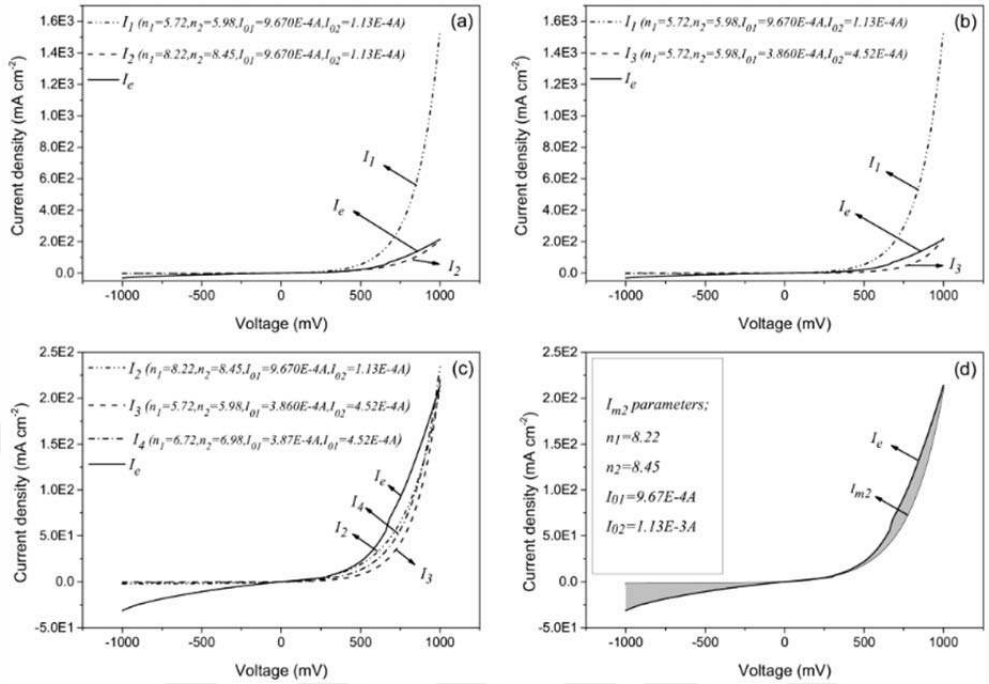

Figure 4.30. I_e and I_1 currents were compared with (a) I_2 and (b) I_3 currents plotted by altering only n_1 and n_2 or I_{01} and I_{02}, respectively. (c) Effects of change in all n_1, n_2, I_{01} and I_{02} were investigated by plotting and comparing I_4 with I_e, I_2 (I_{m2}) and I_3. The resulting I_4 is not as close to the experimental current as I_2. (d) "Filled area curve" comparison of I_e and I_{m2} shows still unmatching regions in detail.

4.4.5. Full model calculation

So far in modeling, I_{01} and I_{02} was roughly determined using dark I-V data. I_{01} and I_{02} can also be calculated using electrostatic parameters and the total diode current can be modeled. It was assumed that the diode was operating under steady-state, so there was only drift, diffusion and thermal recombination-generation currents in the diode. I_{01} and I_{02} currents were calculated employing the following equations

$$I_{01} = \mathrm{q}A\left[\left(\frac{(\mathrm{k}T/\mathrm{q})}{\tau_p}\mu_p\right)^{1/2}\left(\frac{n_i^2}{N_D}\right)\right] \quad (10)$$

$$I_{02} = \mathrm{q}A\left[\left(\frac{n_i}{\sqrt{\tau_n\tau_p}}\right)W\left(\frac{\mathrm{k}T}{3V_{bi}/4}\right)\right] \quad (11)$$

where μ_p is hole mobility (Patel and Ray, 2012), n_i is intrinsic carrier density (1.36E6 cm^{-3}), N_D is donor density (5.83E12 cm^{-3}), V_{bi} is built in potential in the depletion region and W is depletion region width, τ_n and τ_p is electron and hole minority-carrier lifetime, respectively (Hu et al., 2017; Gershon et al., 2013). V_{bi} built in potential was calculated as 395 mV and 27.5 mV using electrostatic Eq. (12)

$$V_{bi} = \frac{E_g}{2\mathrm{q}} + \frac{\mathrm{k}T}{\mathrm{q}}\ln\left(\frac{N_D}{n_i}\right) \quad (12)$$

and capacitance associated depletion region Eq. (13)

$$\frac{1}{C^2} = \frac{2}{qN_DK_S\varepsilon_0A^2}(V_{bi} - V_d) \quad (13)$$

respectively. Here E_g (1.51 eV) is band-gap energy, K_S is dielectric constant (Patel and Ray, 2012), ε_0 is the permittivity of free space, A is junction area (0.294 cm^{-2}) and C is device capacitance at $V_d = 0\ V$ (Fig. 4.31).

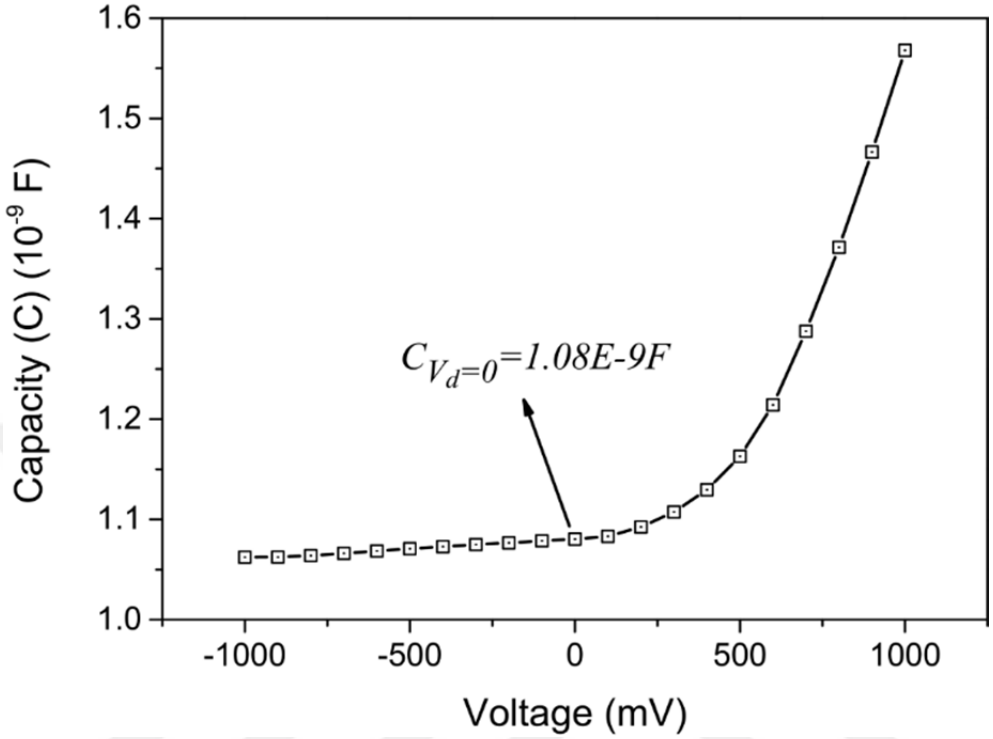

Figure 4.31. The plot of capacitance versus applied voltage. Here V_{bi} built in potential was calculated as 27.5 mV using capacitance associated depletion region Eq. (13) by taking $C = 1{,}08\ nF$ at $V_d = 0\ V$.

I_{01} and I_{02} were calculated as 1.95E-3 A and 6.90E-9 A for $V_{bi} = 395\ mV$ and 1.95E-3 A and 2.62E-8 A for $V_{bi} = 27.5\ mV$, respectively. Therefore, I_1 and I_2 diode currents were plotted using I_{01} and I_{02} couples calculated for two different V_{bi}. The values of n_1 and n_2 were used from as calculated in "*Two exponentials method"* above as 5.72 and 5.98, respectively. V_{bi} related difference in the currents was negligible so I_1 and I_2 diode current plots overlap exactly, but did not match with I_e as depicted in Fig. 4.32(a). By varying n_1 and n_2 to 8.22 and 8.45, respectively, new I_3 current was plotted with I_e as in Fig. 4.32(b).

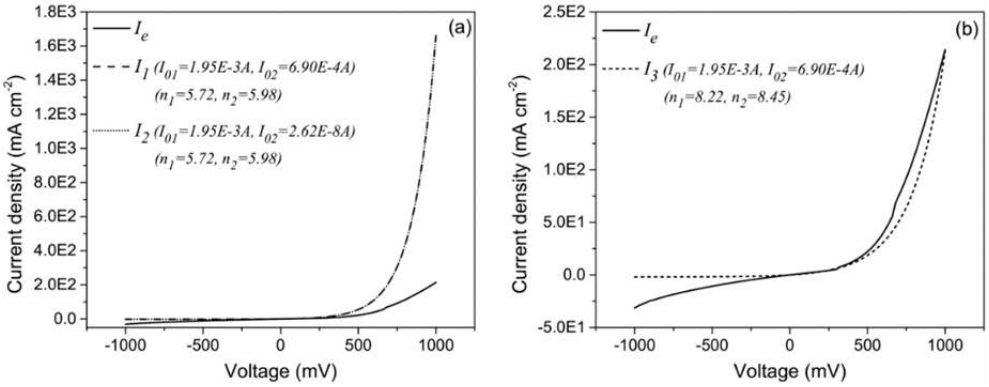

Figure 4.32. Comparison of I_e with calculated (a) I_1 and I_2 currents for two different V_{bi} as $395\,mV$ and $27.5\,mV$, respectively. V_{bi} related difference in the currents was negligible so I_1 and I_2 plots overlap. (b) By varying n_1 and n_2 to 8.22 and 8.45, respectively, new closer I_3 current was plotted with I_e.

The newly calculated I_3 diode current was closer to I_e which confirms the validity of the modeling. However, the curve is still far from modeling the experimental curve, specifically in the negative voltage region. For a more realistic diode model, R_S series resistance; a sum of doping related resistance in quasineutral regions and metal-semiconductor ohmic contact resistances, should be included. Thus, V_d is no longer represents the junction voltage alone. R_S related voltage drop in the junction was modeled as $(V_d - I_d R_S)$ in the exponential expressions. R_S series resistance can be extracted from the slope-over region of the Log(I)-V curve as shown in Fig. 4.33(a) and (b). Voltage variation over current in the slope-over region gives an approximate value of R_S.

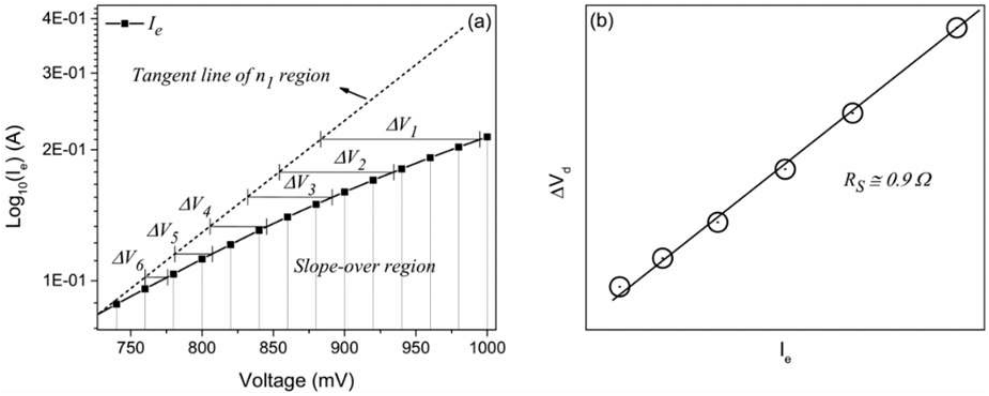

Figure 4.33. (a) V_d voltage variation over I_e current in slope-over region of the Log(I)-V curve. (b) Extraction of R_S from the ratio of ΔV_d to I_e.

Furthermore, $I_{R_{SH}}$ leakage current external to the depletion region flow through a R_{SH} shunt resistance should also be included in the equation as $(V_d - I_d R_S)/R_{SH}$. The final current equation used in the calculation is given below.

$$I_d = I_{01}(\mathrm{e}^{\mathrm{q}(V_d - I_d R_S)/n_1 \mathrm{k}T} - 1) + I_{02}(\mathrm{e}^{\mathrm{q}(V_d - I_d R_S)/n_2 \mathrm{k}T} - 1) + \frac{(V_d - I_d R_S)}{R_{SH}} \quad (14)$$

Eq. (14) can be calculated and plotted using previously calculated I_{01}, I_{02}, R_S and by giving R_{SH} values between 1E6 Ω and 10 Ω. The closest current ($I_{d(R_{SH}=50\,\Omega)}$) to I_e was obtained for $R_{SH} = 50\ \Omega$ is illustrated in Fig. 4.34(a). After this point, the best matching curve can be plotted by trial-and-error method giving the limited values to R_S and R_{SH} i.e. R_S and R_{SH} must be a little lower and higher to push the end of the curve higher and to shift the body, respectively. The best matching curve of I_{m3} current which achieved with $R_S = 0.1\ \Omega$ (Fig. 4.34(b)) and $R_{SH} = 44\ \Omega$ was roughly normalizing the experimental curve (Fig. 4.34(c)). Alternatively, R_S and R_{SH} were extracted as 1.9 and 62 Ω, respectively, from the

voltage dependence of the differential resistance $R_{diff} = \Delta V/\Delta I$ curve in Fig. 4.34(d) (Brus et al., 2016). Although these results are close to the calculated ones, the I_{Rdiff} current plotted using extracted variables gave a characteristic far from the experimental result.

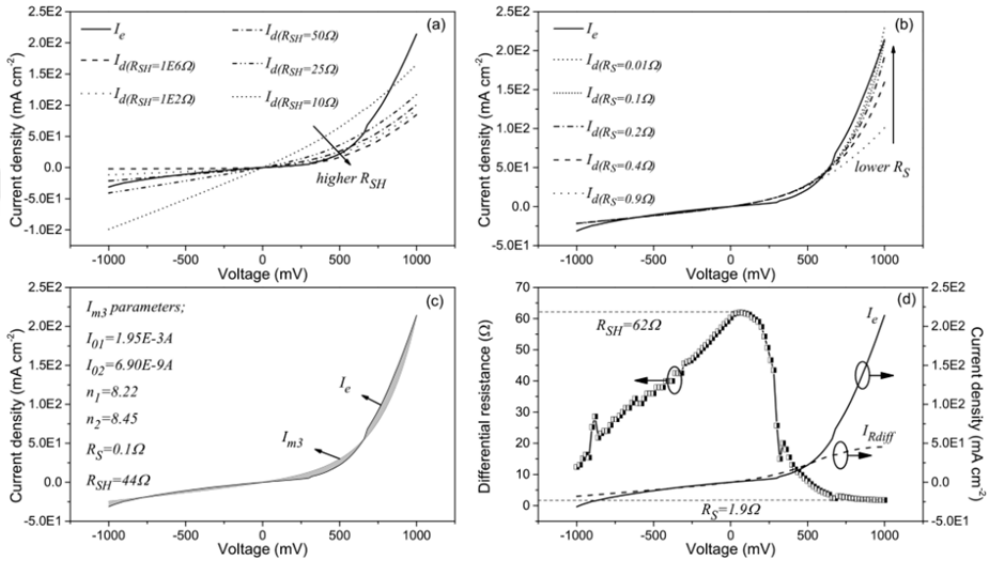

Figure 4.34. Plotting of real diode current was calculated by giving (a) R_{SH} and (b) R_S values between 1E6 Ω and 10 Ω and 0.01 Ω and 0.9 Ω, respectively. Here R_S and R_{SH} must be a little lower and higher to push the end of the curve higher and to shift the body, respectively. (c) The best matching curve of I_{m3} which obtained with $R_S = 0.1\ \Omega$ and $R_{SH} = 44\ \Omega$ was roughly normalizing the experimental curve. (d) Alternative extraction of R_S and R_{SH} as 1.9 and 62 Ω, respectively, from the voltage dependence of the differential resistance $R_{diff} = \Delta V/\Delta I$ curve. New I_{Rdiff} current gave a characteristic far from the experimental result.

4.4.6. Curve fitting

To test the accuracy of the results we calculated above, the diode variables were extracted by applying computer assisted "*Curve fitting"* process to I_e. The previously calculated n_1, n_2, I_{01}, I_{02}, R_S and R_{SH} were used as initial diode variables. Fitting was achieved using OriginPro 9 data analysis and graphing

software. Extracted diode variables $n_1 = 2.62$, $n_2 = 8.45$, $I_{01} = 1\text{E} - 5$ A, $I_{02} = 6.90\text{E} - 9$ A, $R_S = 1.53\ \Omega$ and $R_{SH} = 40.18\ \Omega$ from the fitting process were used to plot I_f fitting current. Fitting curve in Fig. 4.35(a) and I_f plotted in Fig. 4.35(b) exhibit the best but still not perfect matching with I_e. There are still small mismatches between the curves especially at the end of the negative voltage region where the experimental curve moves into the downward direction. Some extracted variables were quite close to the calculated ones which confirm the validity of the calculations.

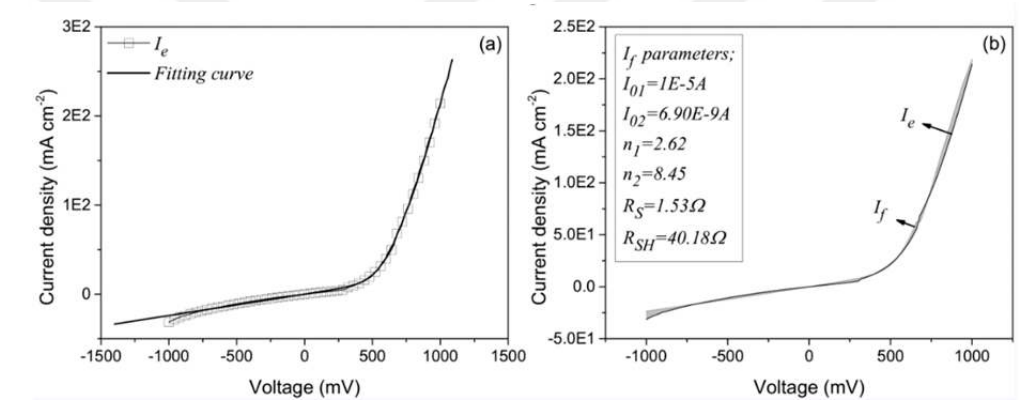

Figure 4.35. (a) Computer assisted "*Curve fitting"* process to I_e. (b) I_f current plotted using variables were extracted from fitting process was compared with I_e.

In Fig. 4.36, the current models acquired from all methods were compared and diode current variables are listed in Table 4.7. I_{m2} modeled in "*Two exponentials method"* using Eq. (5) deliver an imminent curve to the experimental result than I_{m1} modelled in "*Two points method"* using Eq. (1). In other words, a more realistic current model has been achieved by the addition of I_{R-G}. However, there is still a significant mismatch with I_e in the negative region. Both currents revealed almost the same characteristic in the negative region (grey area), non-congruent with the experimental result. Briefly, "*Two points method"* and "*Two exponentials method"* were not sufficient to model the output characteristics of the

diode. On the other hand, it is clear that the curves plotted by changing the value of n instead of I_0 in the current equations present a closer result to the experimental current curve. The curves approached the experimental curve only when n was increased, so the values of n calculated in "*Two points method"* and *"Two exponentials method"* were quite high, because of the current models in Eq. (1) and (5) did not include the R_S and R_{SH} parasitic resistances and only $n\mathrm{k}T/\mathrm{q}$ determines the slope of the curve. Additionally, if the experimental curve was close to ideal, the n values would still not be so large. In real diodes, n_1 and n_2 are a function of voltage in the large and small voltage regions, and are desired to be 1 and 2, respectively (Sah et al., 1957). In fact, the MoS_2/CZTS and ZnO/Ag junctions, which were supposed to be ohmic, revealed Schottky diode characteristics, and a total of more than one diode should be considered in the model. Because of the fabricated diode is far from ideal, possible structural defects create recombination-generation centers such as dislocations, impurity atoms in the crystal lattice and surface defects, the total values of n_1 and n_2 were high in both large and low voltage regions. Therefore, the main current mechanism was dominated by recombination and the dark and illuminated I-V output characteristic of the heterojunction is far from ideal diode and solar cell device. In addition, the impurity of the CZTS crystal causes a low FF value. By including two important variables R_S and R_{SH} to the current equation in "*Full model calculation"* method, the characteristic differences between the plots of I_{m3} and I_e were finally decreased. Although there was no exact match, the two curves were more similar than the previous results. In other words, the real diode current model, which shows characteristic effects of R_S and R_{SH} was successfully acquired. R_S is relatively small as desired. R_{SH}, on the other hand, is undesirably small because of possible structural defects such as impurities at the junction edges. As a result of the small R_{SH}, alternative leakage (shorting) current paths between the junction edges, that is, large recombination currents, are formed and the total diode current and photocurrent curves move away from the ideal. The close results of the calculation in "*Full model calculation"* method and the fitting procedure in "*Curve*

fitting" showed that the calculation method was valid. Therefore, it has been demonstrated that the realistic diode I-V output characteristic can be evaluated by using the electrostatic parameters of the diode.

Table 4.7. Diode current equation variables are achieved in the methods.

	I_{01} (A)	I_{02} (A)	n_1	n_2	R_S (Ω)	R_{SH} (Ω)
Two points method (I_{m1})	9.43E-04		7.12			
Two exponentials method (I_{m2})	9.67E-04	1.13E-03	8.22	8.45		
Full model calculation (I_{m3})	1.95E-03	6.90E-09	8.22	8.45	0.100	44.00
Curve fitting (I_f)	1.00E-05	6.90E-09	2.62	8.45	1.53	40.18

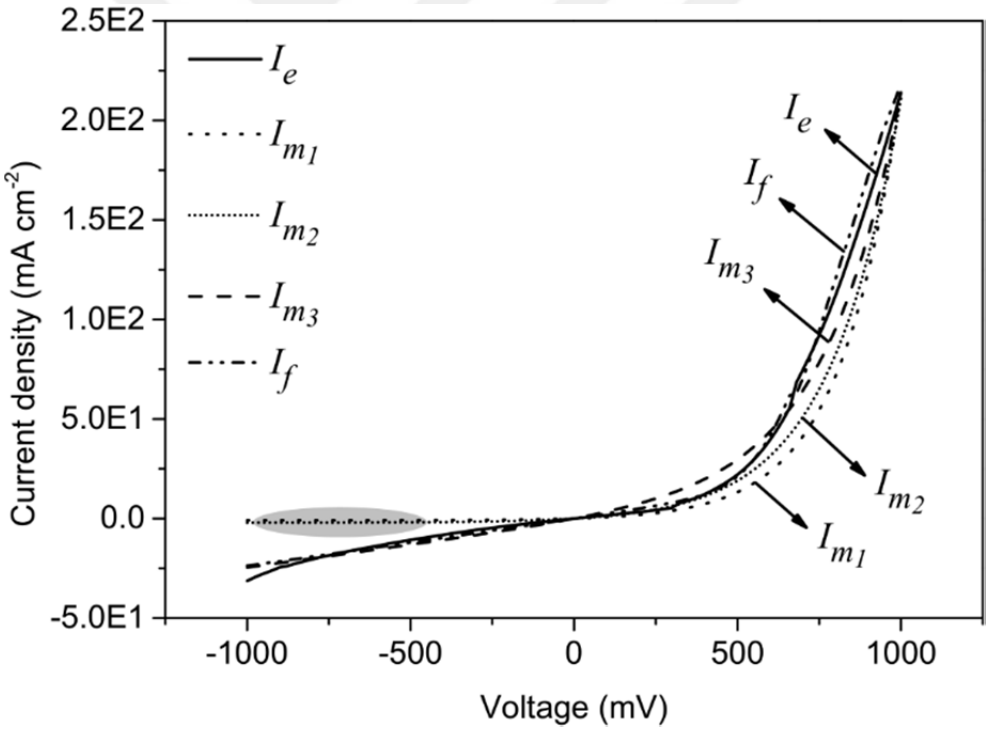

Figure 4.36. The comparison of all CZTS/CdS/ZnO diode current models acquired from all methods. The I_{m3} current obtained by the "*Full model calculation*" method gave the closest result to the experimental current I_e, after the current I_f obtained by the "*Curve fitting*" method.

5. CONCLUSIONS

In the first part of this study, we first studied spin coating and post-heat treatment parameters of CZTS thin films in a comparative way. It has been found that the thickness of the films is inversely proportional to the coating speed, and the change in the amount of precursor and stabilizer in the solution is more effective in controlling the film properties. As the solution molarity decreases, Sn and S loss during annealing in air is further increased and therefore the stoichiometry of the film is degraded. A sudden decrease in the amount of MEA in the solution leads to cracking of the film surface, an increase in S loss and thus undesired phase formations. No significant change was observed in the stoichiometry of the film dried at 300 °C. But the cracks on the film surface reduced and the grain size and consequently the crystallinity also increased. Depending on the increase of annealing temperature in air, the evaporation of the materials increased and the film stoichiometry and hence crystallinity deteriorated. However, when annealing is carried out in N_2, material loss is reduced and there was a very significant improvement in the crystallinity of the film. Finally, by the sulfurization of the films, carbon and oxygen free stoichiometric CZTS thin film absorber layers were fabricated. It has been found that stoichiometric CZTS thin film absorber layers can be prepared under controlled and suitable annealing atmospheres.

In the following study, structural, morphological, optical and electrical properties of the CZTS films were investigated at different annealing temperatures to determine the threshold temperature at which granulation and electronic features tremendously improved. The significant enhancement at main CZTS peaks and crystallite sizes were found at 465 °C which is threshold temperature for the granulation. The morphology of the film began to deteriorate at 580 °C. The sample annealed at 580 °C has the highest material loss which results in a slightly transparent film structure. As a result, lower and upper crystallization threshold

temperature values are found as 465 and 550 °C, respectively. In terms of crystallinity, there was no significant difference between the annealing temperatures of 525, 550 and 580 °C. The best annealing temperature was found as 550 °C in terms of overall film quality. These results provide further evidence that CZTS thin films with large crystallite size are favourable to increase carrier concentration and improve electron transmission.

The influence of annealing temperatures on sol-gel spin coated CZTS thin films in terms of nonlinear optical properties were also investigated. The collected nonlinear optical results seem to be fairly promising for possible implementation in optoelectronics as well for optical switching devices which may enlarge the applications field of this semiconductor. It was seen that the trial solar cell was able to produce photo-current so more efficient devices can be prepared by solving the interface, surface and composition problems that cause the low current and therefore low efficiency.

In the analytical modelling conclusion, the diode current equation of CZTS-based heterojunction was modeled using only dark I-V output data. The equation variables of the diode have been acquired by employing “one exponential”, “two exponentials” and realistic diode equations, respectively. “One exponential” and “two exponentials” equations were not sufficient to model the diode current. The most accurate values of the variables were acquired using the realistic diode current equation. The accuracy of the calculation results has been verified once again by checking with the computer assisted curve fitting process. The structural and interface defects of the device have been successfully investigated using only the variables. This study showed that diode equation variables, which provide inferences about the defects, can be determined even using only I-V output data rather than expensive and complex analysis methods.
Conclusions as list;

* Thicknesses of the films were inversely proportional to the coating speeds.
* Change in the amount of precursor and stabilizer in solution is more effective in controlling the film properties.
* No significant change was observed in the morphology of the film dried between 165 °C and 300 °C.
* By the sulfurization of the films, stoichiometric CZTS thin film absorber layers were fabricated.
* Lower and upper crystallization threshold temperature values are 465 °C and 550 °C, respectively.
* Diode current equation of CZTS-based heterojunction was modelled using only dark I-V output data.
* The equation variables of the diode have been acquired by employing “one exponential”, “two exponentials” and realistic diode equations.
* “One exponential” and “two exponentials” equations were not sufficient to model the diode current.
* The most accurate diode variables were acquired using the realistic diode current equation.
* The accuracy of the electrostatic calculation has been verified by checking with the computer assisted curve fitting process.

BIBLIOGRAPHY

Agawane, G.L., Shin, S.W., Vanalakar, S.A., Suryawanshi, M.P., Moholkar, A.V., Yun, J.H., Gwak, J., and Kim, J.H., (2015). Synthesis of simple, low cost and benign sol–gel Cu_2ZnSnS_4 thin films: influence of different annealing atmospheres, J. Mater. Sci. Mater. Electron. 26: 1900-1907.

Amiria, O., Salavati-Niasarib, M., Sabetb, M., and Ghanbari, D., (2013). Synthesis and characterization of $CuInS_2$ microsphere under controlled reaction conditions and its application in low-cost solar cells, Mater. Sci. Semicond. Process. 16: 1485-1494.

Amiria, O., Salavati-Niasarib, M., Sabetb, M., and Ghanbari, D., (2014). Sonochemical Method for Preparation of Copper Indium Sulfide Nanoparticles and their Application for Solar Cell, Comb. Chem. High Throughput Screen. 17: 183-189.

Awadallah, O., and Cheng, Z., (2017). Formation of sol-gel based CuZnSnS thin films using ppm-level hydrogen sulfide, Thin Solid Films 625: 122-130.

Bär, M., Schubert, B-A., Marsen, B., Krause, S., Pookpanratana, S., Unold, T., Weinhardt, L., Heske, C., and Schock, H-W., (2011). Impact of KCN etching on the chemical and electronic surface structure of Cu_2ZnSnS_4 thin-film solar cell absorbers. Appl. Phys. Lett. 99: 152111.

Berg, D.M., and Dale, P.J., (2014). Kesterites, in: Copper Zinc Tin Sulfide-Based Thin-Film Solar Cells, (Ito, K.,). John Wiley & Sons Ltd. pp. 107-132.

Bonazzi, P., Bindi, L., Bernardini, G.P., and Menchetti, S., (2003). A model for the mechanism of incorporation of Cu, Fe and Zn in the stannite–këesterite series, Cu_2FeSnS_4–Cu_2ZnSnS_4, Can. Mineral. 41: 639-647.

Bouaziz, M., Ouerfelli, J., Amlouk, M., and Belgacem, S., (2007). Structural and optical properties of Cu_3SnS_4 sprayed thin films, Phys. Status Solidi A 204: 3354-3360.

Brus, V.V., Proctor C.M., Ran N.A., and Nguyen T-Q., (2016). Capacitance Spectroscopy for Quantifying Recombination Losses in Nonfullerene Small-Molecule Bulk Heterojunction Solar Cells. Adv. Energy Mater. 6: 1502250.

Chalapathi, U., Kumar, Y.K., Uthanna, S., and Raja, V.S., (2014). Investigations on Cu_3SnS_4 thin films prepared by spray pyrolysis, Thin Solid Films 556: 61-67.

Chaudhuri, T.K., and Tiwari, D., (2012). Earth-abundant non-toxic Cu_2ZnSnS_4 thin films by direct liquid coating from metal–thiourea precursor solution, Sol. Energ. Mat. Sol. Cells 101: 46-50.

Chavda, A., Patel, M., Mukhopadhyay, I., and Ray, A., (2016). Facile, Noncyanide Based Etching of Spray Deposited Cu_2ZnSnS_4 Thin Films for Secondary Phase Removal, ACS SUSTAIN. CHEM. ENG. 4: 2302-2308.

Chen, R., Fan, J., Liu, C., Zhang, X., Shen, Y., and Mai, Y., (2016). Solution-Processed One-Dimensional ZnO@CdS Heterojunction toward Efficient Cu_2ZnSnS_4 Solar Cell with Inverted Structure, Sci. Rep. 6: 35300.

Chen, S.-L., Tao, J., Shu, H.-B., Tao, H.-J., Tang, Y.-X., Shen, Y.-Z., Wang, T., and Pan, L., (2017). Efficient electron transfer kuramite Cu_3SnS_4 nanosheet thin film towards platinum-free cathode in dye-sensitized solar cells, J. Power Sources 341: 60-67.

Cheng, A.-J., Manno, M., Khare, A., Leighton, C., Campbell, S., and Aydil, E., (2011). Imaging and phase identification of Cu_2ZnSnS_4 thin films using confocal Raman spectroscopy, J. Vac. Sci. Technol. A 29: 051203.

Chtouki, T., Taboukhat, S., Kavak, H., Zawadzka, A., Erguig, H., Elidrissi, B., Sahraoui, B., (2019). Characterization and third harmonic generation calculations of undoped and doped spin-coated multilayered CuO thin films, Journal of Physics and Chemistry of Solids 124: 60–66.

Dimitrievska, M., Fairbrother, A., Jawhari, T., Izquierdo-Roca, V., Saucedo, E., and Pérez-Rodríguez, A., (2014a). Multiwavelength excitation Raman scattering study of polycrystalline kesterite Cu_2ZnSnS_4 thin films, Appl. Phys. Lett. 104: 021901.

Dimitrievska, M., Xie, H., Fairbrother, A., Fontané, X., Gurieva, G., Saucedo, E., Pérez-Rodríguez, A., Schorr, S., and Izquierdo-Roca, V., (2014b). Multiwavelength excitation Raman scattering of $Cu_2ZnSn(S_xSe_{1-x})_4$ ($0 \leq x \leq 1$) polycrystalline thin films: Vibrational properties of sulfoselenide solid solutions, Appl. Phys. Lett. 105: 031913.

Dong, L., Cheng, S., Lai, Y., Zhang, H., and Jia, H., (2017). Sol-gel processed CZTS thin film solar cell on flexible molybdenum foil, Thin Solid Films 626: 168-172.

Feng, W., Han, J., Ge, J., Peng, X., Liu, Y., Jian, Y., Yuan, L., Xiong, X., Cha, L., and Liao, C., (2017). Influence of Annealing Temperature on CZTS Thin Film Surface Properties, J. Electron. Mater. 46: 288-295.

Fernandes, P., Salomé, P., and Cunha, A., (2010). A study of ternary Cu_2SnS_3 and Cu_3SnS_4 thin films prepared by sulfurizing stacked metal precursors, J. Phys. D: Appl. Phys. 43: 215403.

Fernandes, P.A., Salomé, P.M.P., and Cunha, A.F., (2011). Study of polycrystalline Cu_2ZnSnS_4 films by Raman scattering, J. Alloys Compd. 509: 7600–7606.

Fontané, X., Izquierdo-Roca, V., Saucedo, E., Schorr, S., Yukhymchuk, V.O., Valakh, M.Y., Pérez-Rodríguez, A., and Morante, J.R., (2012). Vibrational properties of stannite and kesterite type compounds: Raman scattering analysis of $Cu_2(Fe,Zn)SnS_4$, J. Alloys Compd. 539: 190-194.

Foo, K.L., Kashif, M., Hashim, U., and Liu, W-W., (2014). Effect of different solvents on the structural and optical properties of zinc oxide thin films for optoelectronic applications. Ceram. Int. 40: 753-761.

Ganguly, J., Saha, S., Bera, A., and Ghosh, M., (2017). Exploring electro-optic effect and third-order nonlinear optical susceptibility of impurity doped quantum dots: Interplay between hydrostatic pressure, temperature, and noise, Opt. Commun. 387: 166–173.

Ge, J., Wu, Y., Zhang, C., Zuo, S., Jiang, J., Ma, J., Yang, P., and Chu, J., (2012). Comparative study of the influence of two distinct sulfurization ramping rates on the properties of Cu_2ZnSnS_4 thin films, Appl. Surf. Sci. 258: 7250-7254.

Gershon, T., Shin, B., Bojarczuk, N., Gokmen, T., Lu, S., and Guha, S., (2013). Photoluminescence characterization of a high-efficiency Cu_2ZnSnS_4 device. J. Appl. Phys. 114: 154905.

Ghediya, P.R., Chaudhuri, T.K., and Patel, K., (2016). Temperature dependence electrical conduction of solution-processed CZTS films in dark and under light, in: IOP Conference Series: Materials Science and Engineering, IOP Publishing, pp. 012162.

Green, M.A., 2000. Power to the people: sunlight to electricity using solar cells, UNSW Press, New South Wales, 93 p.

Green, M.A., 2006. Consolidation of thin-film photovoltaic technology: the coming decade of opportunity, Prog.Photovolt:Res. Appl. 14(5): 383-392.

Gubler, U., and Bosshard, C., (2000). Optical third-harmonic generation of fused silica in the gas atmosphere: Absolute value of the third-order nonlinear optical susceptibility $\chi^{(3)}$, Phys. Rev. B 61: 10702.

Guc, M., Levcenko, S., Bodnar, I.V., Izquierdo-Roca, V., Fontane, X., Volkova, L.V., Arushanov, E., and Pérez-Rodríguez, A., (2016). Polarized Raman scattering study of kesterite type Cu_2ZnSnS_4 single crystals, Sci. Rep. 6: 19414.

Guo, X., Han, J., Zhang, H., Lv, X., Yan, J., and Sun, R., (2017). Sol-gel synthesis of CuZnSnS thin films under mild conditions, J. Alloys Compd. 697: 361-366.

Hall, S., Szymanski, J., and Stewart, J., (1978). Kesterite, Cu<2) (Zn, Fe) SnS<4), and stannite, Cu<2) (Fe, Zn) SnS<4), structurally similar but distinct minerals, Can. Mineral. 16: 131-137.

Hergert, F., and Hock, R., (2007). Predicted formation reactions for the solid-state syntheses of the semiconductor materials Cu_2SnX_3 and Cu_2ZnSnX_4 (X=S, Se) starting from binary chalcogenides, Thin Solid Films 515: 5953-5956.

Hu, L., Patterson, R.J., Hu, Y., Chen, W., Zhang, Z., Yuan, L., Chen, Z., Conibeer, G.J., Wang, G., and Huang, S., (2017). High Performance PbS Colloidal Quantum Dot Solar Cells by Employing Solution-Processed CdS Thin Films from a Single-Source Precursor as the Electron Transport Layer. Adv. Funct. Mater. 27: 1703687.

Islam, S., Hossain, M., Kabir, H., Rahaman, M., Bashar, M., Gafur, M., Kabir, A., Bhuiyan, M., Ahmed, F., and Khatun, N., (2015). Optical, Structural and Morphological Properties of Spin Coated Copper Zinc Tin Sulfide Thin Films, Int. J. Thin. Fil. Sci. Tec. 4:155-161.

Ito, K., and Nakazawa, T., (1988). Electrical and optical properties of stannite-type quaternary semiconductor thin films, Jpn. J. Appl. Phys. 27: 2094.

Kajzar, F., Okada-Shudo, Y., Meritt, C., and Kafafi, Z., (2001). Second- and third-order non-linear optical properties of multilayered structures and composites of C_{60} with electron donors, Synth. Met. 117: 189–193.

Kato, T., Handa, A., Yagioka, T., Matsuura, T., Yamamoto, K., Higashi, S., Wu, J.-L., Tai, K.F., Hiroi, H., Yoshiyama, T., Sakai, T., Sugimoto, H., (2017). Enhanced efficiency of Cd-free $Cu(In,Ga)(Se,S)_2$ minimodule via (Zn,Mg)O second buffer layer and alkali post treatment, 44th IEEE Photovoltaic Specialists Conference, Washington DC, 25–30 June 2017.

Kazuya, M., Kunihiko, T., Yuya, N., and Hisao, U., (2011). Annealing Temperature Dependence of Properties of Cu_2ZnSnS_4 Thin Films Prepared by Sol–Gel Sulfurization Method, Jpn. J. Appl. Phys. 50:05FB08.

Khalil, M.I., Bernasconi, R., Ieffa, S., Lucotti, A., Le Donne, A., Binetti, S., and Magagnin, L., (2015). Effect of co-electrodeposited Cu-Zn-Sn precursor compositions on sulfurized CZTS thin films for solar cell, ECS Trans. 64: 33-41.

Khalkar, A., Lim, K.-S., Yu, S.-M., Patole, S.P., and Yoo, J.-B., (2013). Effect of growth parameters and annealing atmosphere on the properties of Cu_2ZnSnS_4 thin films deposited by cosputtering, Int. J. Photoenergy 2013: 7 pages.

Kim, H.T., Kim, D., and Park, C., (2012). Temperature effects on Cu_2ZnSnS_4 (CZTS) films deposited by spraying method, Mol. Cryst. Liq. Cryst. 564: 155-161.

Kubodera, K., and Kobayashi, H., (1990). Determination of Third-Order Nonlinear Optical Susceptibilities for Organic Materials by Third-Harmonic Generation, Mol. Cryst. Liq. Cryst. Inc. Nonlinear Opt. 182(1): 103–113.

Kumar, M., Dubey, A., Adhikari, N., Venkatesan, S., and Qiao, Q., (2015a). Strategic review of secondary phases, defects and defect-complexes in kesterite CZTS–Se solar cells, Energy Environ. Sci. 8: 3134-3159.

Kumar, M., Dubey, A., Adhikari, N., Venkatesan, S., and Qiao, Q., (2015b). Strategic review of secondary phases, defects and defect-complexes in kesterite CZTS–Se solar cells. Energy Environ. Sci. 8: 3134- 3159.

Kunihiko, T., Noriko, M., Masatoshi, O., and Hisao, U., (2008). Pre-Annealing of Precursors of Cu_2ZnSnS_4 Thin Films Prepared by Sol–Gel Sulfurizing Method, Jpn. J. Appl. Phys. 47: 598.

Kuo, S-Y. and Hsieh, M-Y., (2014). Efficiency enhancement in Cu2ZnSnS4 solar cells with subwavelength grating nanostructures, Nanoscale 6: 7553-7559.

Li, J.B., Chawla, V., and Clemens, B.M., (2012). Investigating the Role of Grain Boundaries in CZTS and CZTSSe Thin Film Solar Cells with Scanning Probe Microscopy, Adv. Mater. 24: 720-723.

Li, W., Chen, J., Yan, C., Liu, F., and Hao, X., (2014). Transmission electron microscopy analysis for the process of crystallization of Cu_2ZnSnS_4 film from sputtered Zn/CuSn precursor, Nanotechnology 25: 195701.

Lin, X., Steigert, A., Lux-Steiner, M.C., Ennaoui, A., (2012). One-step solution-based synthesis and characterization of kuramite Cu_3SnS_4 nanocrystals, RSC Adv. 2: 9798-9800.

Liu, X., Feng, Y., Cui, H., Liu, F., Hao, X., Conibeer, G., Mitzi, D. B., and Green, M., 2016. The current status and future prospects of kesterite solar cells: a brief review, Prog. Photovolt: Res. Appl. 24 (6): 879–898.

Maeda, K., Tanaka, K., Nakano, Y., and Uchiki, H., (2011). Annealing temperature dependence of properties of Cu_2ZnSnS_4 thin films prepared by sol–gel sulfurization method, Jpn. J. Appl. Phys. 50:05FB08.

Majula, L., Mlyuka, N., Samiji, M., Bryce, R., Kim, D., Kim, S., Lee, H., Choi, H., (2015). Spin-coated kesterite CZTS thin films for photovoltaic applications, J. Korean Phys. Soc. 67: 1078-1081.

Maker, P.D., Terhune, R.W., Nisenoff, M., and Savage, C.M., (1962). Effects of Dispersion and Focusing on the Production of Optical Harmonics, Phys. Rev. Lett. 8: 21–22.

Mkawi, E., Ibrahim, K., Ali, M., and Mohamed, A.S., (2013). Dependence of copper concentration on the properties of Cu_2ZnSnS_4 thin films prepared by electrochemical method, Int. J. Electrochem. Sci. 8: 359-368.

Monserrat, B., Park, J-S., Kim, S., and Walsh, A., (2018). Role of electron-phonon coupling and thermal expansion on band gaps, carrier mobility, and interfacial offsets in kesterite thin-film solar cells. Appl. Phys. Lett. 112: 193903.

Muhunthan, N., Singh, O.P., Singh, N.V., Sood, K.N. and Rashmi, (2015a). Electric field-effect-assisted persistent photoconductivity in CZTS, Adv. Mater. Lett. 6: 290-293.

Muhunthan,N., Singh, O.P., Toutam, V., and Singh, V.N., (2015b). Electrical characterization of grain boundaries of CZTS thin films using conductive atomic force microscopy techniques, Mater. Res. Bull. 70: 373-378.

Muska, K., Kauk, M., Altosaar, M., Pilvet, M., Grossberg, M., and Volobujeva, O., (2011). Synthesis of Cu_2ZnSnS_4 monograin powders with different compositions, Energy Procedia, 10: 203-207.

Nguyen, T.T.T., Shin, H.-Y., Kim, G.Y., Kim, J.R., Jo, W., Yoon, S., Lee, K.D., and Kim, J.Y., (2015). Raman scattering studies of Cu_2ZnSnS_4 thin films: Local distribution of the secondary phase $Cu_{2-x}S$ and the effect of KCN etching on $Cu_{2-x}S$, J. Korean Phys. Soc. 66: 117-122.

Olekseyuk, I.D., Dudchak, I.V., and Piskach, L.V., (2004). Phase equilibria in the Cu_2S–ZnS–SnS_2 system, J. Alloys Compd. 368:135-143.

Paire, M., Delbos, S., Vidal, J., Naghavi, N., Guillemoles, J.F., (2014). Chalcogenide Thin-Film Solar Cells, in: G. Conibeer, A. Willoughby (Eds.) Solar Cell Materials: Developing Technologies, John Wiley & Sons, Ltd, Chichester, UK, pp. 145-215.

Park, H., Hwang, Y.H., and Bae, B.-S, (2013). Sol–gel processed Cu_2ZnSnS_4 thin films for a photovoltaic absorber layer without sulfurization, JSST, 65: 23-27.

Park, J-S., Kim, S., Hood, S.N., and Walsh, A., (2018). Open-circuit voltage deficit in Cu_2ZnSnS_4 solar cells by interface bandgap narrowing. Appl. Phys. Lett. 113: 212103.

Park, S.-N., Sung, S.-J., Son, D.-H., Kim, D.-H., Gansukh, M., Cheong, H., and Kang, J.-K., (2014). Solution-processed Cu_2ZnSnS_4 absorbers prepared by appropriate inclusion and removal of thiourea for thin film solar cells, RSC Adv. 4: 9118-9125.

Patel, M., and Ray, A., (2012). Enhancement of output performance of Cu_2ZnSnS_4 thin film solar cells—A numerical simulation approach and comparison to experiments. Physica B Condens. Matter. 407: 4391-4397.

Sah, C., Noyce, R.N., and Shockley, W., (1957). Carrier Generation and Recombination in P-N Junctions and P-N Junction Characteristics. in Proceedings of the IRE 45: 1228-1243.

Schubert, B.A., Marsen, B., Cinque, S., Unold, T., Klenk, R., Schorr, S., and Schock, H.-W., (2011). Cu_2ZnSnS_4 thin film solar cells by fast coevaporation, Prog. Photovolt. Res. Appl. 19: 93–96.

Scragg, J.J., Ericson, T., Kubart, T., Edoff, M., and Platzer-Björkman, C., (2011). Chemical Insights into the Instability of Cu_2ZnSnS_4 Films during Annealing, Chem. Mater. 23: 4625-4633.

Shiyani, T., Patel, M., Mukhopadhyay, I., Ray, A., (2016). Effect of Annealing on Structural Properties of Electrodeposited CZTS Thin Films, IETE Tech. Rev. 33: 2-6.

Song, X., Ji, X., Li, M., Lin, W., Luo, X., and Zhang, H., (2014). A review on development prospect of CZTS based thin film solar cells, Int. J. Photoenergy 2014:11.

Su, Z., Tan, J.M.R., Li, X., Zeng, X., Batabyal, S.K., and Wong, L.H., (2015). Cation Substitution of Solution-Processed Cu_2ZnSnS_4 Thin Film Solar Cell with over 9% Efficiency, Adv. Energy Mater. 5: 1500682.

Sun, K., Yan, C., Liu, F., Huang, J., Zhou, F., Stride, J.A., Green, M., and Hao, X., (2016). Over 9% Efficient Kesterite Cu_2ZnSnS_4 Solar Cell Fabricated by Using $Zn_{1-x}Cd_xS$ Buffer Layer, Adv. Energy Mater. 6: 1600046.

Swami, S.K., Kumar, A., and Dutta, V., (2013). Deposition of kesterite Cu_2ZnSnS_4 (CZTS) thin films by spin coating technique for solar cell application, Energy Procedia 33: 198-202.

Tajima, S., Itoh, T., Hazama, H., Ohishi, K., and Asahi, R., (2015). Improvement of the open-circuit voltage of Cu_2ZnSnS_4 solar cells using a two-layer structure, Appl. Phys. Express 8: 082302. [57] Xu, J., (2016). Investigation of Cu_2ZnSnS_4 thin-film solar cells with carrier concentration gradient, J. Phys. Chem. Solids 98: 32-37.

Tanaka, K., Fukui, Y., Moritake, N., and Uchiki, H., (2011). Chemical composition dependence of morphological and optical properties of Cu_2ZnSnS_4 thin films deposited by sol–gel sulfurization and Cu_2ZnSnS_4 thin film solar cell efficiency, Sol. Energ. Mat. Sol. Cells 95: 838-842.

Tanaka, K., Moritake, N., Oonuki, M., and Uchiki, H., (2008). Pre-annealing of precursors of Cu_2ZnSnS_4 thin films prepared by sol–gel sulfurizing method, Jpn. J. Appl. Phys. 47: 598-601.

Tanaka, K., Oonuki, M., Moritake, N., and Uchiki, H., (2009). Cu_2ZnSnS_4 thin film solar cells prepared by non-vacuum processing, Sol. Energ. Mat. Sol. Cells 93: 583-587.

Tanaka, T., Yoshida, A., Saiki, D., Saito, K., Guo, Q., Nishio, M., Yamaguchi, T., (2010). Influence of composition ratio on properties of Cu_2ZnSnS_4 thin films fabricated by co-evaporation, Thin Solid Films 518: S29-S33.

Tao, H., Cao, F., Zhang, C., Chen, S., Tan, B., and Tao, J., (2017). In-situ growth of CuZnSnS nanoparticles on thiol reduce graphene oxide for CuZnSnS-sensitized solar cells, J. Alloys Compd. 698: 114-120.

Teeter, G., Du, H., Leisch, J., Young, M., Yan, F., Johnston, S., Dippo, P., Kuciauskas, D., Romero, M., Newhouse, P., (2010). Combinatorial study of thin-film Cu_2ZnSnS_4 synthesis via metal precursor sulfurization, in: 35th Photovoltaic Specialists Conference (PVSC), IEEE, pp. 000650-000655.

Tunuguntla, V., Chen, W.-C., Shih, P.-H., Shown, I., Lin, Y.-R., Hwang, J.-S., Lee, C.-H., Chen, L.-C., and Chen, K.-H., (2015). A nontoxic solvent based sol-gel Cu_2ZnSnS_4 thin film for high efficiency and scalable low-cost photovoltaic cells, J. Mater. Chem. A, 3: 15324-15330.

Valakh, M.Y., Kolomys, O.F., Ponomaryov, S.S., Yukhymchuk, V.O., Babichuk, I.S., Izquierdo-Roca, V., Saucedo, E., Perez-Rodriguez, A., Morante, J.R., Schorr, S., and Bodnar, I.V., (2013). Raman scattering and disorder effect in Cu_2ZnSnS_4, Phys. Status Solidi Rapid Res. Lett. 7: 258-261.

Walsh A., Chen, S., Gong, X., Wei, S.H., Ihm, J., and Cheong, H., (2011). Crystal structure and defect reactions in the kesterite solar cell absorber Cu_2ZnSnS_4 (CZTS): theoretical insights, in: AIP Conference Proceedings, AIP, pp. 63-64.

Wang, W., Shen, H., Wong, L.H., Su, Z., Yao, H., and Li, Y., (2016). A 4.92% efficiency Cu_2ZnSnS_4 solar cell from nanoparticle ink and molecular solution, RSC Adv. 6: 54049-54053.

Wang, W., Winkler, M.T., Gunawan, O., Gokmen, T., Todorov, T.K., Zhu, Y., and Mitzi, D.B., (2014). Device Characteristics of CZTSSe Thin-Film Solar Cells with 12.6% Efficiency, Adv. Energy Mater. 4: 1301465.

Weber, A., Krauth, H., Perlt, S., Schubert, B., Kötschau, I., Schorr, S., and Schock, H.W., (2009). Multi-stage evaporation of Cu_2ZnSnS_4 thin films, Thin Solid Films, 517: 2524-2526.

Weber, A., Mainz, R., and Schock, H., (2010). On the Sn loss from thin films of the material system Cu–Zn–Sn–S in high vacuum, J. Appl. Phys. 107: 013516.

Wei, S.-Y., Liao, Y.-C., Hsu, C.-H., Cai, C.-H., Huang, W.-C., Huang, M.-C., and Lai, C.-H., (2016). Achieving high efficiency $Cu_2ZnSn(S,Se)_4$ solar cells by non-toxic aqueous ink: Defect analysis and electrical modeling, Nano Energy 26: 74-82.

Wei, Z., Newman, M.J., Tsoi, W.C., and Watson, T.M., (2016). Raman mapping analysis for removal of surface secondary phases of CZTS films using chemical etching. Appl. Phys. Lett. 109: 123902.

Xinkun, W., Wei, L., Shuying, C., Yunfeng, L., and Hongjie, J., (2012). Photoelectric properties of Cu_2ZnSnS_4 thin films deposited by thermal evaporation, J. Semicond. 33: 022002.

Yeh, M.Y., Lee, C.C., and Wuu, D.S., (2009). Influences of synthesizing temperatures on the properties of Cu_2ZnSnS_4 prepared by sol–gel spin-coated deposition, J. Sol-Gel Sci. Technol. 52: 65-68.

Yeh, M.-Y., Lei, P.-H., Lin, S.-H., and Yang, C.-D., (2016). Copper-Zinc-Tin-Sulfur Thin Film Using Spin-Coating Technology, Materials 9: 526.

Yin, X., and Gong, H., (2012). Heat-field-stimulated decomposition reaction in Cu_2ZnSnS_4, Acta Mater. 60: 6732-6741.

Yu, X., Ren, A., Wang, F., Wang, C., Zhang, J., Wang, W., Wu, L., Li, W., Zeng, G., Feng, L., (2014a). Synthesis and characterization of CZTS thin films by sol-gel method without sulfurization, Int. J. Photoenergy 2014: 861249.

Yu, Y., Ge, J., Prabhakar, T., and Yan, Y., (2014b). Effects of spin speed on the properties of spin-coated Cu_2ZnSnS_4 thin films and solar cells based on DMSO solution, in: 40th Photovoltaic Specialist Conference (PVSC), IEEE, pp. 0448-0451.

Zawadzka, A., Płóciennik, P., Strzelecki, J., and Sahraoui, B., (2014). Transparent amorphous zinc oxide thin films for NLO applications, Opt. Mater. 37: 327–337.

Zhang, X., Wu, H., Fu, E., and Wang, Y., (2019). In-Depth Characterization of Secondary Phases in Cu_2ZnSnS_4 Film and Its Application to Solar Cells. Nanomaterials, 9(6): 855.

Zhuk, S., Kushwaha, A., Wong, T.K.S., Masudy-Panah, S., Smirnov, A., and Dalapati, G.K., (2017). Critical review on sputter-deposited Cu_2ZnSnS_4 (CZTS) based thin film photovoltaic technology focusing on device architecture and absorber quality on the solar cells performance, Sol. Energ. Mat. Sol. Cells, 171: 239-252.

CURRICULUM VITAE

Teoman ÖZDAL graduated from B.S. in the Department of Electrical Technical Teacher from the Fırat University. After that, he started to MSc in the Department of Electrical Electronics Engineering from the Mustafa Kemal University. Following his MSc graduation, he started to PhD in the Department of Physics from the Cukurova University. His research interests are thin film crystals, physical properties of p-n junctions, and semiconductor solar cells.